

(2)

NAVAL POSTGRADUATE SCHOOL Monterey, California

AD-A237 234




THESIS

DTIC
ELECTE
JUN 21 1991
S B D

EQUATORIAL ENTRAINMENT
ZONE SIMULATIONS

by

Chi-Shao Chen

June, 1990

Thesis Advisor:
Second Reader:

Roland W. Garwood
Pecheng Chu

Approved for public release; distribution is unlimited

91 6 18 031

91-02442


UNCLASSIFIED

SECURITY CLASSIFICATION OF THIS PAGE

REPORT DOCUMENTATION PAGE				Form Approved OMB No 0704-0188	
1a REPORT SECURITY CLASSIFICATION Unclassified			1b RESTRICTIVE MARKINGS		
2a SECURITY CLASSIFICATION AUTHORITY			3 DISTRIBUTION/AVAILABILITY OF REPORT Approved for public release; distribution is unlimited		
2b DECLASSIFICATION/DOWNGRADING SCHEDULE					
4 PERFORMING ORGANIZATION REPORT NUMBER(S)			5 MONITORING ORGANIZATION REPORT NUMBER(S)		
6a NAME OF PERFORMING ORGANIZATION Naval Postgraduate School		6b OFFICE SYMBOL (If applicable) 440	7a NAME OF MONITORING ORGANIZATION Naval Postgraduate School		
6c ADDRESS (City, State, and ZIP Code) Monterey, CA 93943-5000			7b ADDRESS (City, State, and ZIP Code) Monterey, CA 93943-5000		
8a NAME OF FUNDING SPONSORING ORGANIZATION		8b OFFICE SYMBOL (If applicable)	9 PROCUREMENT INSTRUMENT IDENTIFICATION NUMBER		
8c ADDRESS (City, State, and ZIP Code)			10 SOURCE OF FUNDING NUMBERS		
			PROGRAM ELEMENT NO	PROJECT NO	TASK NO
					WORK UNIT ACCESSION NO
11 TITLE (Include Security Classification) EQUATORIAL ENTRAINMENT ZONE SIMULATIONS					
12 PERSONAL AUTHOR(S) CHEN, CHI-SHAO					
13a TYPE OF REPORT Master's Thesis		13b TIME COVERED FROM _____ TO _____		14 DATE OF REPORT (Year, Month, Day) JUNE 1990	
15 PAGE COUNT 89					
16 SUPPLEMENTARY NOTATION The views expressed in this thesis are those of the author and do not reflect the official policy or position of the Department of Defense or the U.S. Government					
17 COSAT CODES			18 SUBJECT TERMS (Continue on reverse if necessary and identify by block number)		
FIELD	GROUP	SUB-GROUP	air-sea interaction, equatorial circulation		
19 ABSTRACT (Continue on reverse if necessary and identify by block number)					
<p>The equatorial entrainment zone model of Garwood <i>et al.</i> (1989) is employed along with data collected by Moum <i>et al.</i> (1984) during the Tropic Heat I Experiment to explain how the dissipation of turbulence is related to surface forcing of wind stress and net heat flux. Four numerical experiments with different atmospheric conditions are conducted with the entrainment zone model. Solar radiation is diurnally repeated, and wind stress is held constant in the first case. The model is forced with linearly varied wind speed in the second case and uses observed winds for the third case. The first three cases demonstrated the effects of wind stress on the dissipation of turbulence. In the final case both observed wind and observed solar radiation were applied to the model to simulate the effect of realistic forcing, allowing a comparison between model-predicted and observed values of dissipation. Numerical solutions qualitatively agree with the observations, and the time and depth dependence of the diurnal dissipation cycle are well reproduced by the model.</p>					
20 DISTRIBUTION/AVAILABILITY OF ABSTRACT <input checked="" type="checkbox"/> UNCLASSIFIED UNLIMITED <input type="checkbox"/> SAME AS RPT <input type="checkbox"/> DTIC USERS			21 ABSTRACT SECURITY CLASSIFICATION unclassified		
22a NAME OF RESPONSIBLE INDIVIDUAL Roland W. Garwood			22b TELEPHONE (Include Area Code) (408) 646-3260		22c OFFICE SYMBOL 68 CD

DD Form 1472, JUN 86

Previous editions are obsolete

SECURITY CLASSIFICATION OF THIS PAGE

S/N 0102-LF-014-6603

UNCLASSIFIED

Approved for public release; distribution is unlimited

Equatorial Entrainment Zone Simulations

by

Chi-Shao Chen
Lieutenant Commander, Chinese Navy
B.S., Chinese Naval Academy, 1978

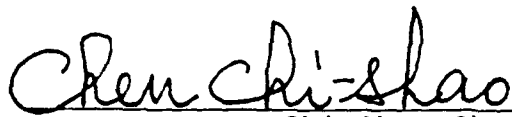
Submitted in partial fulfillment of the
requirements for the degree of

MASTER OF SCIENCE IN PHYSICAL OCEANOGRAPHY

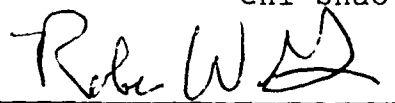
from the

NAVAL POSTGRADUATE SCHOOL
June 1990


Author:


Chi-Shao Chen

Approved by:


Roland W. Garwood, Thesis Advisor


Pecheng Chu, Second Reader


Curtis A. Collins, Chairman
Department of Oceanography

ABSTRACT

The equatorial entrainment zone model of Garwood et al. (1989) is employed along with data collected by Moum et al. (1984) during the Tropic Heat I Experiment to explain how the dissipation of turbulence is related to surface forcing of wind stress and net heat flux. Four numerical experiments with different atmospheric conditions are conducted with the entrainment zone model. Solar radiation is diurnally repeated, and wind stress is held constant in the first case. The model is forced with linearly varied wind speed in the second case and uses observed winds for the third case. The first three cases demonstrated the effects of wind stress on the dissipation of turbulence. In the final case both observed wind and observed solar radiation were applied to the model to simulate the effect of realistic forcing, allowing a comparison between model-predicted and observed values of dissipation. Numerical solutions qualitatively agree with the observations, and the time and depth dependence of the diurnal dissipation cycle are well reproduced by the model.



iii

Accession For	
NTIS GRA&I	<input checked="checked" type="checkbox"/>
DTIC TAB	<input type="checkbox"/>
Unannounced	<input type="checkbox"/>
Justification	
by	
Distribution/	
Availability Codes	
Dist	Avail and/or Special
A-1	

TABLE OF CONTENTS

I.	INTRODUCTION	1
A.	PURPOSE OF THE STUDY	1
B.	STATEMENT OF PROBLEM	2
C.	LITERATURE REVIEW	5
	1. Equatorial Circulation	5
	2. Atmospheric Conditions	8
	3. Air-Sea Interaction	9
	4. Equatorial Zonal Momentum	10
II.	THEORY	12
A.	EQUATORIAL ENTRAINMENT MODEL	12
B.	MEAN TURBULENT KINETIC ENERGY EQUATION	13
C.	MODEL EQUATIONS	14
	1. Dynamic Stability Requirement and Mixing Hypothesis	14
	2. Momentum and Heat Equations	16
	3. Steady State Solution	16
	4. Dissipation Calculation	18
D.	UNSTEADY RESPONSE TO DIURNAL SURFACE BUOYANCY FLUX	18
III.	MODEL SIMULATIONS AND DISCUSSIONS	19
A.	CASE 1	21
B.	CASE 2	24
C.	CASE 3	28

D.	CASE 4	34
E.	COMPARISON AND SUMMARY	38
IV.	SUMMARY AND RECOMMENDATIONS	70
	REFERENCES	73
	INITIAL DISTRIBUTION LIST	76

LIST OF TABLES

TABLE I.	DAILY INFORMATION ON WIND SPEED (U_{10}), MAXIMUM VALUE OF DOWNWARD MOMENTUM FLUX, MAXIMUM VALUE OF DISSIPATION RATE (e_{max}), DEPTH OF MAXIMUM DISSIPATION ($z_{e=max}$), DEPTH RANGE OF DISSIPATION ($z_{e=0}$), AND DEPTH OF EUC JET ($z_{u=max}$) BASED ON PROFILES OF CASE 2.	27
TABLE II.	DAILY INFORMATION BASED ON CASE 3. SOME SECONDARY MAXIMUM DISSIPATION VALUES ARE LISTED IN PARENTHESIS.	31
TABLE III.	A LISTING OF MAXIMUM (MINIMUM) DISSIPATION RATE, ITS DEPTH, AND WIND SPEED BASED ON DISSIPATION CONTOURS OF CASE 3.	32
TABLE IV.	LISTING OF DISSIPATION AT THREE DIFFERENT DEPTHS IN CASES 3 AND 4	37
TABLE V.	AVERAGED VERTICAL INTEGRAL OF DISSIPATION FOR EACH HOUR IN CASE 4	39

LIST OF FIGURES

Figure 1.	Typical equatorial temperature profile observed at 140°W. Dotted portion under 150m depth is artificial and not relevant to this study.	40
Figure 2.	Typical zonal velocity profile on equator observed at 140°W. Dotted portion under 150m depth is artificial and not relevant to this study.	40
Figure 3.	Net downward surface heat flux for prescribed first three cases.	40
Figure 4.	Bidaily model-predicted profiles of zonal velocity ($\bar{u}(z)$ solid line m/sec), temperature ($\bar{T}(z)$ dotted line degree C), downward momentum flux ($-\bar{u}'w'(z)$ dashed line m^2/sec^2), and dissipation ($\epsilon(z)$ chaindot line m^2/sec^3) for case 1.	41
Figure 5.	Bihourly model-predicted profiles of zonal velocity ($\bar{u}(z)$ solid line m/sec), temperature ($\bar{T}(z)$ dotted line degree C), downward momentum flux ($-\bar{u}'w'(z)$ dashed line m^2/sec^2), and dissipation ($\epsilon(z)$ chaindot line m^2/sec^3) for day 12 of case 1.	42
Figure 6.	Predicted vs. t and z daily dissipation for case 1. The contour increment is $2 \times 10^{-7} m^2/sec^3$	44
Figure 7.	Surface forcing conditions and vertical integral of dissipation for case 1. (a) Constant wind speed of $\bar{u}_{10} = 5.7$ m/sec is shown. (b) Wind stress is constant value of $0.05 N/m^2$. (c) Sum of simulated solar radiation and backradiation is periodically cycled every day. (d) Vertical integral of dissipation shows a clearly diurnal dissipation cycle.	46

- Figure 8. Surface forcing conditions and vertical integral of dissipation for case 2. (a) Wind speed is held constant value of 6 m/sec for 4 days. From day 5 to day 8, the wind speed is linearly increased to 10.8 m/sec then it is linearly decreased to 1.1 m/sec for the period from day 9 to day 12. (b) The wind stress calculated from equation 3-1. (c) Net surface heat flux is the same as in case 1. (d) Vertical integral of dissipation. 47
- Figure 9. Bidaily model-predicted profiles of zonal velocity ($\bar{U}(z)$ solid line m/sec), temperature ($\bar{T}(z)$ dotted line degree C), downward momentum flux ($-\bar{u'w'}$ (z) dashed line m^2/sec^2), and dissipation (ϵ (z) chaindot line m^2/sec^3) for case 2. 48
- Figure 10. Bihourly model-predicted profiles of zonal velocity ($\bar{U}(z)$ solid line m/sec), temperature ($\bar{T}(z)$ dotted line degree C), downward momentum flux ($-\bar{u'w'}$ (z) dashed line m^2/sec^2), and dissipation (ϵ (z) chaindot line m^2/sec^3) for day 8 of case 2. 49
- Figure 11. Bihourly model-predicted profiles of zonal velocity ($\bar{U}(z)$ solid line m/sec), temperature ($\bar{T}(z)$ dotted line degree C), downward momentum flux ($-\bar{u'w'}$ (z) dashed line m^2/sec^2), and dissipation (ϵ (z) chaindot line m^2/sec^3) for day 9 of case 2. 51
- Figure 12. Bihourly model-predicted profiles of zonal velocity ($\bar{U}(z)$ solid line m/sec), temperature ($\bar{T}(z)$ dotted line degree C), downward momentum flux ($-\bar{u'w'}$ (z) dashed line m^2/sec^2), and dissipation (ϵ (z) chaindot line m^2/sec^3) for day 12 of case 2. 53
- Figure 13. Predicted daily dissipation vs time and depth for case 2. The contour increment is $2 \times 10^{-7} m^2/sec^3$. The bold line has the value of $2 \times 10^{-6} m^2/sec^3$ 55

Figure 14.	Surface forcing conditions of (a) recorded wind speed, (b) wind stress, (c) and net surface heat flux as in previous cases and (d) vertical integral of dissipation for case 3.	57
Figure 15.	Bidaily model-predicted profiles of zonal velocity ($\bar{u}(z)$ solid line m/sec), temperature ($\bar{T}(z)$ dotted line degree C), downward momentum flux ($-\bar{u'w'}$ (z) dashed line m^2/sec^2), and dissipation ($\epsilon(z)$ chaindot line m^2/sec^3) for case 3.	58
Figure 16.	Bihourly model-predicted profiles of zonal velocity ($\bar{u}(z)$ solid line m/sec), temperature ($\bar{T}(z)$ dotted line degree C), downward momentum flux ($-\bar{u'w'}$ (z) dashed line m^2/sec^2), and dissipation ($\epsilon(z)$ chaindot line m^2/sec^3) for day 12 of case 3.	59
Figure 17.	Predicted daily dissipation vs. t and z for case 4. The contour increment in $2 \times 10^{-7} m^2/sec^3$	61
Figure 18.	Surface forcing conditions and vertical integral dissipation for case 4. (a) and (b) are the same as for case 3. (c) The net surface heat flux. (d) Vertical integral of dissipation showing a lower value of dissipation in the day time. . . .	63
Figure 19.	Bidaily model-predicted profiles of zonal velocity ($\bar{u}(z)$ solid line m/sec), temperature ($\bar{T}(z)$ dotted line degree C), downward momentum flux ($-\bar{u'w'}$ (z) dashed line m^2/sec^2), and dissipation ($\epsilon(z)$ chaindot line m^2/sec^3) for case 4.	64
Figure 20.	Bihourly model-predicted profiles of zonal velocity ($\bar{u}(z)$ solid line m/sec), temperature ($\bar{T}(z)$ dotted line degree C), downward momentum flux ($-\bar{u'w'}$ (z) dashed line m^2/sec^2), and dissipation ($\epsilon(z)$ chaindot line m^2/sec^3) for day 12 of case 4.	65
Figure 21.	Predicted daily dissipation vs t and z for case 4. The contour increment is $2 \times 10^{-7} m^2/sec^3$	67

- Figure 22 Depth averaged dissipation (10-110 m)
observed in the Tropic I Experiment in
November 1984 at equator, 140 W. The
large ticks on the abscissa represent
1200 GMT (0200 LT). Hourly winds from
shipboard measurement are superimposed.
(Moum et al., 1989). 69
- Figure 23. Ensemble averages of depth-averaged
dissipation for each hour of the day from
the dissipation observations in the Tropic
Heat I Experiment in November 1984
(Moum et al., 1989). 69

I. INTRODUCTION

A. PURPOSE OF THE STUDY

Although the dynamic and thermal structure of the oceanic planetary boundary layer (OPBL) is generally understood in most regions of the globe, the structure of the OPBL at the equator has not been well explained. The oceanic mixed layer's response to atmospheric forcing is determined principally by local thermodynamic processes and turbulent mixing processes. However, there are significant differences near the equator. Considerable research effort has been devoted to improving the physical understanding and to developing mathematical solutions. However, before the Tropical Heat I Experiment of 1984, model development was limited because of sparse microstructure data at the equator.

Right on the equator there exists the eastward flowing Equatorial Undercurrent (EUC) beneath the westward flow of the South Equatorial Current (SEC). The upper equatorial waters have a steady, large, vertical shear of zonal velocity and very energetic turbulence. Because of the large vertical shear above the EUC core, the equatorial mixing layer is also characterized by a very thick entrainment zone with a shallower, weakly stratified surface layer. This differs from the mid-latitude mixed layer system where usually there is a

very thin entrainment zone with a well-mixed surface layer of usually greater thickness.

The main purpose of this study is to understand how the dissipation rate (ϵ) for ocean turbulence at the equator is related to the local atmospheric conditions of surface heat flux and wind stress. The equatorial entrainment zone model of Garwood et al. (1989) was employed, along with data collected during the Tropical Heat I Experiment. This data consists of temperature and current velocity profiles and a time-varying 12-day zonal wind speed record collected near 140 W longitude in the equatorial Pacific ocean by Moum et al. (1989).

A statement of the problem is contained in section B of this chapter, detailing the scientific objectives of the study. In section C the background literature is reviewed. Chapter II gives the mathematical basis of the model and the physical interpretation and assumptions. Chapter III shows the results of four different numerical solutions and discusses the significance of the results. Finally, Chapter IV states the conclusions and recommendations for the study.

B. STATEMENT OF PROBLEM

For years, geophysicists and mathematicians have been fascinated by the equatorial ocean because of the absence of the Coriolis force ($f=0$) and the presence of the EUC (Equatorial Undercurrent). The conventional view of equatorial dynamics requires that the zonal wind stresses be balanced by

the vertical integral of the zonal pressure gradient, the mesoscale eddy flux and the mean advection over the upper few hundred meters. Our understanding of the dynamics in this region has been severely hindered by lack of observed data. Intense hydrographic surveys and turbulent kinetic energy dissipation rate measurements taken at the equator near 140°W during the Tropical Heat I Experiment in November 1984 revealed unforeseen surface layer structure, and a diurnal cycle of the dissipation rate was noted, confirming the earlier report of Paka and Fedorov.

The vertical temperature profile at the equator shows a shallow, weakly stratified surface layer with a depth of 10-30 meters in contrast to a typical convectively well-mixed layer. Moum *et al.* (1989) defined the mixing layer (ML) as a surface layer in which the variation in dissipation was small. Additionally, equatorial profiles of temperature reveal a large entrainment zone with a thickness of 80-120 meters, whereas in other areas of the open ocean the entrainment zone is a relatively thin thermocline. Because of its thick entrainment zone, the equator is an ideal place for studying turbulent mixing processes associated with entrainment.

An equatorial entrainment zone model has been derived by Garwood *et al.* (1989). By prescribing diurnal surface heat fluxes and a constant westward wind stress component and zonal pressure gradient, solutions for this model simulate the EUC,

the typical equatorial temperature profile, and a diurnal cycle of the dissipation rate.

Garwood (1987) showed that maximum entrainment zone thickness (δ) is proportional to the friction velocity divided by the Coriolis parameter when the entrainment zone achieves a steady state. At the equator, although the Coriolis force equals zero, the Ekman suction of the easterly trade winds causes a positive mean upwelling velocity. This results in a large, ($\delta=100$ m) steady entrainment zone beneath a shallow surface layer (Garwood et al., 1990).

Peters and Gregg (1988) and Moum et al. (1989) suggested that the diurnal cycle of dissipation was caused by a high frequency night-time burst of breaking internal waves. However, in Garwood's model the diurnal dissipation cycle can be simulated with no special consideration of internal waves.

The model solution compares favorably with a section observed across the equator at 140° 15' W from 3°N to 3°S for four days in November 1984 (Moum et al., 1986) and qualitatively shows that the maximum dissipation rate corresponds to: (a) upward heat flux (night time); (b) large wind stress; (c) greater vertical shear (above EUC core); and (d) possibly, kinetic energy provided by internal waves.

In this thesis, in order to understand how the upper layer of the ocean responds to atmospheric forcing, the Equatorial Entrainment Zone Model was initialized with the typical

temperature and velocity profile observed during the Tropical Heat I Experiment (Moum et al., 1989). Several numerical experiments were then conducted. The first case was run with constant wind stress and periodic solar radiation have a local noon time peak of 800 W/m^2 . The result showed a diurnal dissipation cycle and an equilibrium state was reached approximately after five days. The second case was designed to determine the effect of a linear increase and decrease in wind speed upon the mixing processes. The third case employed the time-varying wind stress that was observed for the 12-day period 20 November to 1 December, 1984. The radiation was cyclical, but repeated exactly every day for this case. The last case employed both observation of solar radiation and wind data from the Tropic Heat I cruise to specify the surface boundary conditions. Predictions of dissipation for this last case were then compared to the observed dissipation.

C. LITERATURE REVIEW

1. Equatorial Circulation

From observations, the equatorial currents are characterized by zonal bands in which the flow is alternately eastward and westward (Knauss, 1963). The eastward flowing countercurrent approximately located between 5°N and 10°N is the North Equatorial Countercurrent (NECC). The South Equatorial Countercurrent (SECC) is between 5°S to 10°S . Here

"countercurrent" refers to the flow direction being counter to the direction of the easterly trade winds. The westward flow between the two countercurrents is called the South Equatorial Current (SEC). During the northern summer the NECC is in its northernmost position, whereas in the northern winter the current lies closest to the equator. Wyrтки (1978) demonstrated that dynamic height differences and geostrophic transport indices correlate extremely well for each of the four equatorial currents, making surface slope an excellent indicator of the geostrophic transport. Also, his computations of mean geostrophic transports for the individual currents identify the SEC as the strongest flow, transporting 55×10^6 m³/sec (Wyrтки, 1984)

Cromwell et al. (1952) discovered the Pacific EUC to be a subsurface eastward flow that is about 100-200 m thick and 200-300 km wide. It is centered approximately on the equator with its core just beneath the base of the mixed layer in the top of the equatorial thermocline. During GATE (GARP Atlantic Tropical Experiment), Duing et al. (1975) found evidence for a meandering of the Atlantic Equatorial Undercurrent with a period of 2-3 weeks and a zonal wavelength of 3,200 km. Firing (1987) observed a complex system of deep zonal currents in the central equatorial Pacific during 16 months of current measurements spanning the 1982-1983 El Nino episode. At least three extraequatorial currents appear to be permanent: the

north and south intermediate countercurrents, with eastward velocity cores at 600 m depth, located 1.5-2.0 degrees from the equator; and the south equatorial intermediate current, with a westward core at 900 m depth three or more degrees south of the equator. On the equator, the deep jets were nearly stationary during the period of his measurements.

The discovery of the EUC triggered much equatorial modeling activity. Almost all of the early equatorial models included baroclinic effects and assumed the surface layer to be decoupled from the deeper ocean (Yoshida, 1959; Stommel, 1960; Charney, 1960). The first successful extension of classical Ekman theory to the equator was Stommel's model which balances the Coriolis force with the vertical diffusion of momentum and the horizontal pressure gradient. The zonal pressure gradient is a source of eastward momentum that drives the undercurrent. The wind forcing is added to the ocean as a surface stress and a zero stress condition is imposed at the bottom of the layer. If the eddy viscosity is constant with the depth, the vertical structure of the zonal velocity at the equator is parabolic, with surface flow in the direction of the wind and subsurface flow (undercurrent) in the opposite direction. In addition, the model develops a meridional circulation similar to that diagnosed from the distribution of tracers in the Equatorial Pacific. Stommel (1960) showed there is surface divergence of fluid from the equator, subsurface convergence, and equatorial upwelling.

2. Atmospheric Conditions

At low altitudes, between the two subtropical high-pressure belts, the variability is much less and, except on infrequent occasions, the circulation pattern on any day varies little from the average for the season (Neiburger et al., 1982). Furthermore, Gray (1976) determined that there was cyclogenesis near the equator, using tropical cyclone origin location data for 20 years (Elsberry et al., 1989). Since the horizontal component of the Coriolis force vanishes at the equator, the winds are geostrophic.

The streamline analysis by Palm  n and Newton (1969) shows that the trade winds are the steadiest feature of the atmospheric circulation near the surface. Although the easterly trades are subject to fluctuation, the westward wind stress component is observed year-round at the equator.

Although the equatorial surface water is cooled by the upwelling, the sea surface temperature (SST) is generally greater than 25  C, and the mean annual precipitation rate is larger than 2,000 millimeters in the equatorial western Pacific Ocean and between 500-1000 millimeters in the equatorial eastern Pacific Ocean (Tchernia, 1980). During the 1984 Tropic Heat I Experiment, average solar radiation for 12 days shows the maximum short wave heating at local noon may reach 950 W/m² and net longwave back radiation is about 150 W/m². Seasonal variation of the Intertropical Convergence Zone

(ITCZ) causes it to be close to the equator in the northern hemispheric winter when the cumulus clouds block much of the solar heating.

3. Air-Sea Interaction

The atmosphere is heated more by the earth's water and land surface (44%) than by the direct absorption of solar radiation (<20%). The Earth's surface heats the atmosphere in three general ways: longwave radiation, sensible heat flux, and latent heat flux. Because of the heat that is given to the atmosphere, available potential energy is created and converted into kinetic energy by means of the buoyancy forces causing the rising of warm air and sinking of cold air. The kinetic energy of the atmosphere is then partly passed back to the ocean by wind stress driven ocean currents. Turbulent motions are generated at the interface of the two media by conversion of mean kinetic energy (KE) to turbulent kinetic energy (TKE) and by buoyant convection.

The mixing processes in the OPBL occur because of the turbulence. Laminar fluid is affected by the generation and transport of turbulent kinetic energy which tends to homogenize the fluid. One criterion for examining dynamic instability is the gradient Richardson number, a non-dimensional number arising in the study of shearing flows of a stratified fluid. This number is the ratio of work done against gravitational stability to energy transferred from mean to turbulent motion. Theoretical studies have placed the

critical Richardson number variously from 1/4 to 2 (Huschke, 1959).

The first mixed layer model was proposed by Krauss and Turner in 1967. This early model dealt with the heat budget and the mechanical energy budget, using concepts of heat conservation and a TKE equation to form a closed model system. This model can be tuned to give an explanation of physical processes. In this study, the Equatorial Entrainment Zone Model contains similar considerations. However, in the equatorial region, the closure technique is different.

4. Equatorial Zonal Momentum

The most important contributions to the zonal momentum budget at the equator are the zonal convergence of zonal momentum, upwelling of eastward momentum, the zonal pressure gradient, the divergence of the mesoscale eddy flux, and the turbulent stress (Bryden and Brady 1985). Balancing these factors can give a steady-state conservation equation:

$$\bar{u} \frac{\partial \bar{u}}{\partial x} + \bar{w} \frac{\partial \bar{u}}{\partial z} = - \frac{1}{\rho} \frac{\partial \bar{p}}{\partial x} - \frac{\partial}{\partial x} \overline{u'u'} - \overline{u'v'} - \frac{\partial}{\partial z} \overline{u'w'} \quad (1.1)$$

where \bar{u} and \bar{v} are mean zonal and meridional velocities, \bar{p} is the mean pressure, ρ is density, x is the zonal direction (positive eastward), and $\overline{u'w'}$ is the vertical turbulent flux of zonal momentum. In the Tropic Heat I Experiment, the large numbers of profiles collected make it possible to calculate approximate balances of the momentum budget (Dillon and Moum 1989). However, Dillon and Moum did not find an expected large

scale momentum balance by using typical estimates of the large scale forces and conventional estimates of the turbulent stress. They suspected either the large scale processes during the time of measurement were highly atypical, or estimates of momentum flux based on a production-dissipation balance are flawed. A similar result was reported by McPhaden et al. (1988) who studied the response of the upper equatorial Pacific to a westerly wind burst of several days duration and estimated that the eddy viscosity necessary to explain the observations would be on the order of $100 \text{ cm}^2/\text{s}$; this is much larger than Gregg et al. (1985) estimated using microstructure measurements. In this case they suggested the eddy viscosity and turbulent stress estimated from dissipation rate and shear measurements must be treated with caution.

II. THEORY

A. EQUATORIAL ENTRAINMENT MODEL

The Equatorial Entrainment Zone Model is based upon a dynamic stability hypothesis to the entrainment zone below the equatorial mixed layer. In the form used here, it presumes meridional-symmetric heat (1st law of thermodynamics) and momentum budgets, together with the mixing hypothesis to get solutions.

The model uses a vertical grid with 5 m resolution spanning the region $z=0$ to $z=300$ m. A time step of 1 hour is adequate to resolve diurnal-period changes. The mixing of heat and momentum on this grid is achieved with the method developed by Adamec et al. (1981). This method was used interactively each time step to achieve convergence (Garwood, 1990).

Generally, the oceanic boundary layer or mixed layer is a fully turbulent region that is bounded above by the air-ocean interface, and where the temperature and salinity are usually observed to be fairly well mixed. The limitation of ocean mixed layer depth (MLD) is usually determined by the Obukhov length scale $L=(\tau/\rho)^{3/2}/B_0$, under the influence of wind stress τ and downward buoyancy flux B_0 , where ρ is density. Off the equator, and in the case of negligible surface buoyancy flux (neutral conditions), the limiting scale for the MLD may be

Rossby and Montgomery's neutral planetary boundary scale u_* / f (1935), where u_* is the ocean surface frictional velocity and $f=2 \Omega_z$ is the Coriolis parameter. This scale may also be a dominate scale for the entrainment zone immediately below the surface layer. Although L is the limiting scale for the surface layer, u_* / f may determine the potential maximum thickness δ_{max} of the underlying entrainment zone. Garwood (1987) showed that $\delta_{max}=0.2u_* / f$ when the entrainment zone achieves a steady state.

Near the equator, the complexity of the mixed layer system creates a structure unique from other ocean regions. Here, upwelling may reduce the thickness of the surface layer to a fraction of the Obukhov length (Muller et al., 1984). The Naval Postgraduate School OPBL Bulk Model (NPS MODEL) (Garwood, 1977) yields typical equatorial ML depths of 10-30 m. Since the thickness of the equatorial entrainment zone δ is much larger than the depth of surface layer h , the magnitude of h is not very significant for the entrainment zone solutions. Therefore, in this study h will be taken to be a representative value of 20 m for all cases.

B. MEAN TURBULENT KINETIC ENERGY EQUATION

The steady state meridional-symmetric mean turbulent kinetic energy equation is:

$$\frac{d\bar{E}}{dt} = \overset{I}{-\overline{u'w'}} \frac{\partial \bar{U}}{\partial z} - \overset{II}{\frac{\overline{w'\rho'}g}{\rho_o}} - \overset{III}{\frac{\partial}{\partial z} \left[\overline{w' \left(E + \frac{\rho'}{\rho_o} \right)} \right]} - \overset{IV}{e} = 0 \quad (2.1)$$

where $E = \frac{1}{2} (\overline{u'^2} + \overline{v'^2} + \overline{w'^2})$.

Term I represents the rate of mechanical production which is the dominate source of TKE in wind driven regimes. This term is the conversion of mean kinetic energy to turbulent kinetic energy. Term II is the buoyancy flux and can be either a source or a sink in TKE. In nighttime with net surface heat loss the mixed layer buoyancy flux will be positive, generating more TKE enhancing the vertical mixing processes. Term III is the divergence of the turbulent flux of TKE and is responsible for transporting turbulence generated near the surface to the bottom of the mixed layer. The Term IV represents viscous dissipation. Dissipation into heat is a major sink for TKE.

C. MODEL EQUATIONS

1. Dynamic Stability Requirement and Mixing Hypothesis

Without forcing, the entrainment zone is expected to remain dynamically stable. The two processes that can destabilize the entrainment zone are: (a) a net input of mechanical energy from the overlying mixed layer and (b) enhancement of the mean kinetic energy available for generation of turbulence, caused by a convergence of the mean flow ($\frac{\partial \bar{w}}{\partial z} < 0$) in the presence of the mean shear ($\frac{\partial \bar{u}}{\partial z}$) above the

equatorial undercurrent core. With these processes, the model for the entrainment zone invokes two hypotheses. First, there will be no significant turbulent fluxes of mass, momentum, or buoyancy unless the gradient Richardson number, R_i is less than a critical value. Second, if a dynamic instability is initiated, the mixing coefficients of all conservative properties are assumed to be proportional, and vertical fluxes of momentum ($\overline{u'w'}$) and buoyancy ($\alpha g \overline{\theta'w'}$) will be just sufficient to maintain the R_i at the stable limit (Garwood, 1990), that is:

$$\frac{\alpha g \frac{\partial \overline{\theta}}{\partial z}}{\left(\frac{\partial \overline{u}}{\partial z}\right)^2} \geq R_{icr} \quad (2.2)$$

where R_{icr} in this model equals 1/4.

The condition of proportional mixing coefficients for momentum and buoyancy is equivalent to having the flux Richardson number R_f be proportional to the gradient Richardson number R_i .

$$\frac{R_i}{R_f} = \gamma_{cr} = \frac{\overline{u'w'}}{\overline{\theta'w'}} \quad (2.3)$$

where $R_f = \frac{\alpha g \overline{\theta'w'}}{\overline{u'w'} \frac{\partial \overline{u}}{\partial z}}$, and the dimensionless ratio γ_{cr} may also be interpreted as the ratio of eddy viscosity to eddy conductivity. This ratio is approximately 0.74 for neutral conditions, and it is variable for turbulent regimes of different stabilities. However, it approaches a constant value of order unity in the stable limit for the transition from

turbulent to laminar flow (Garwood 1990). In this model we use $\gamma_{cr} = 1$.

2. Momentum and Heat Equations

The mean momentum and heat budgets for the meridionally-symmetric entrainment zone at the equator are:

$$\frac{\partial \bar{u}}{\partial t} = -\frac{1}{\rho} \frac{\partial \bar{p}}{\partial x} - \frac{\partial \overline{u'w'}}{\partial z} - \bar{w} \frac{\partial \bar{u}}{\partial z} - \bar{u} \frac{\partial \bar{u}}{\partial x} \quad (2.4)$$

$$\frac{\partial \bar{\theta}}{\partial t} = -\frac{\partial \overline{\theta'w'}}{\partial z} - \bar{w} \frac{\partial \bar{\theta}}{\partial z} - \bar{u} \frac{\partial \bar{\theta}}{\partial x} \quad (2.5)$$

where $\bar{\theta}$ is mean potential temperature, $\overline{u'w'}$ is vertical eddy momentum flux, and $\overline{\theta'w'}$ is vertical eddy heat flux.

If large scale zonal gradients of \bar{u} , $\bar{\theta}$, and \bar{p} are independently specified, then equations (2.2), (2.3) together with the momentum and heat equation (2.4), (2.5) constitute a closed system of equations for $\frac{\partial \overline{u'w'}}{\partial z}$, $\frac{\partial \overline{\theta'w'}}{\partial z}$, $\frac{\partial \bar{u}}{\partial z}$ and $\frac{\partial \bar{\theta}}{\partial z}$.

3. Steady State Solution

In steady state, the system may be combined to give 1st-order differential equations for turbulent fluxes.

$$\frac{\partial \overline{u'w'}}{\partial z} = P - \frac{\alpha g}{\gamma_{cr} R_{icr}} \bar{w} \left(\frac{\overline{\theta'w'}}{\overline{u'w'}} \right) \quad (2.6)$$

$$\frac{\partial \overline{\theta'w'}}{\partial z} = -\frac{\alpha g}{\gamma_{cr}^2 R_{icr}} \bar{w} \left(\frac{\overline{\theta'w'}}{\overline{u'w'}} \right)^2 \quad (2.7)$$

where P is the pressure gradient. Mean shear and mean temperature estimates can be obtained when these equations are solved for $\overline{u'w'}(z)$ and $\overline{\theta'w'}(z)$.

$$\frac{\partial}{\partial z} \bar{u} = \frac{\alpha g}{\gamma_{cr} R_{icr}} \left(\frac{\overline{\theta'w'}}{\overline{u'w'}} \right) \quad (2.8)$$

$$\frac{\partial}{\partial z} \bar{\theta} = \frac{\alpha g}{\gamma_{cr}^2 R_{icr}} \left(\frac{\overline{\theta'w'}}{\overline{u'w'}} \right)^2 \quad (2.9)$$

Bryden and Brady (1985), and Dillon et al. (1989) suggested a Gaussian function for P by neglecting the zonal advection:

$$P = \frac{1}{\rho} \frac{\partial \bar{p}}{\partial x} = g \eta_x [e^{-(z/D)^2}] \quad (2.10)$$

where $D=135$ m and the zonal surface slope η_x is on the order of 10^{-7} (Garwood, 1990). For added realism in the unsteady simulation, the solution includes the undercurrent core and the region below, down to 300 m below the surface. To include the region, $w(z)$ is exponentially induced with depth, giving a vertical dependence similar to that of Muller and Roth (1986).

$$\bar{w}(z) = -\bar{w}_h \frac{z e^{z/H}}{H e^{-1}} \quad (2.11)$$

where $H = 75$ m.

Because H is compared to δ , the turbulent fluxes of momentum and heat into the top of the entrainment zone are approximately equal to the surface value.

$$\overline{u'w'}_{(z=H)} = u_*^2 \quad (2.12)$$

$$\overline{\theta'w'}_{(z=H)} = \frac{Q_o}{\rho C_p} \quad (2.13)$$

For the steady state case in the model $u_* = 0.01$ m/s and $Q_o = 100$ W/m² (Garwood, 1990).

4. Dissipation Calculation

Assuming no significant external source of energy (such as gravity waves propagating vertically from above or below the entrainment zone), all the terms of the TKE equation can be computed. In particular, dissipation can be shown to be proportional to the buoyancy flux in the entrainment zone (Garwood, 1990).

$$\epsilon = \alpha g \overline{\theta'w'} \left[1 - \frac{1}{\gamma_{cr} R_{icr}} \right] \quad (2.14)$$

D. UNSTEADY RESPONSE TO DIURNAL SURFACE BUOYANCY FLUX

After achieving a steady state solution, the imposition of a diurnally oscillating surface buoyancy flux causes a transient period of adjustment in the modeled ocean. The model mixed layer entrainment zone system requires a few days to again achieve a near equilibrium state. The diurnal response to the dissipation of TKE below the mixed layer falls to near zero from about three hours after sunrise until almost sunset. Dissipation is both depth and time dependent. The time of maximum dissipation occurs later as depth increases, and peak dissipation at $z=-120$ m does not occur until just before sunrise. This phase shift with depth for the response to the surface buoyancy flux is due to storage effects in the mean buoyancy and mean kinetic energy (Garwood, 1990).

III. MODEL SIMULATIONS AND DISCUSSIONS

In order to understand the role of dissipation in the equatorial region, the EEZM (equatorial entrainment zone model) is used to study the dependence of dissipation on surface forcing, time, and depth. Typical temperature and zonal velocity profiles measured during the Tropical Heat I Experiment in November 1984 are assigned as initial conditions for the model system (Figure 1 and Figure 2). For a 12-day period during November 1984, wind, solar radiation, and dissipation were observed near 0°N , 140°W . In this study, four different numerical calculations of the momentum and heat equation (equations 2.4, 2.5) were made:

1. Using a constant wind stress and a diurnal solar radiation, this run shows that a nearly equilibrium state is reached after five days and a diurnal cycle is well simulated.
2. This run uses periodic solar radiation and a linear increase or decrease of wind speed to note differences in mixing processes.
3. After an equilibrium state is reached, this run uses time-dependent forcing dictated by recorded wind data and simulated periodic solar radiation to verify wind stress effects.
4. After an equilibrium state is reached, this run uses forcing dictated by both recorded wind and recorded solar radiation data to calculate the value of dissipation for comparison with the observations.

The daytime heating due to solar shortwave radiation is assumed as follows: sunrise is at 6:00 a.m., sunset is at 6:00

p.m., and a maximum solar radiation is at local noon. Nighttime solar shortwave heating is assigned a value of zero. The back radiation from the sea surface to the air is given an average value of 150 W/m^2 as measured in the November 1984 cruise from Moum et al. (1986). For all four cases, the time is treated as local time, which differs from the study of Moum et al. (1986) where Greenwich Mean Time (GMT) was used. Day 1 hour 0 in this thesis corresponds to 1000 GMT, November 19, 1984.

The model predicts the value of the vertical integral of dissipation as a function of atmospheric conditions and initial vertical profiles of \bar{T} and \bar{u} . The dissipation integral ($\int \epsilon dz$) provides a measure of atmospheric forcing effects. The profiles are plotted every 2 days at hour 24, since dissipation is larger in the nighttime, to show the correlations between temperature $\bar{T}(z)$, zonal velocity $\bar{u}(z)$, vertical momentum flux $\overline{u'w'}(z)$, and dissipation $\epsilon(z)$. For the final day (day 12), the profiles are plotted every 2 hours in order to present a daily cycle for comparison. Contouring is used to give time and depth dependence of dissipation $\epsilon(z, t)$.

Figure 1, the initial temperature profile, shows a shallow mixed layer (5 m) with a temperature of 25°C . Beneath the mixed layer \bar{T} varies nonlinearly down to a depth of 130 m. Below 130 m there is a relatively constant temperature lapse rate. Figure 2 shows the initial zonal velocity profile. The upper 25 m flows to the west with a maximum speed of 0.3

m/sec, corresponding to the SEC. The lower portion region with eastward flow with a maximum velocity of 1.41 m/sec at 120 m depth, represents the EUC.

A. CASE 1

In this case, the model was forced with simple atmospheric conditions. The wind stress was held constant for the whole period with a value of 5×10^{-2} N/m² (Newtons per meter square). Solar radiation was cycled periodically everyday with a peak value of 800 W/m² (Watts per meter square) at local noon, and longwave back radiation was assigned a constant value of 150 W/m². The net downward surface heat flux plus radiation yields a gain in the daytime and net heat loss in the nighttime as shown in Figure 3. Here the nighttime is defined as 6:00 p.m. to 6:00 a.m. and is a period of constant heat loss at the rate of 150 W/m². From 6:00 a.m., net heating increases to a maximum value of 650 W/m² at local noontime then decreases to zero again at 6:00 p.m.

The vertical profiles predicted by the model (Figure 4) show that sea surface temperature dropped from an initial value of greater than 25°C to less than 24°C in day 11. Dissipation occurs where the vertical momentum flux is positive. Because the zonal velocity increases with depth ($\frac{\partial \bar{u}}{\partial z} < 0$) above the EUC core, a negative (downward) momentum flux ($-\overline{u'w'} < 0$) is necessary because the shear production in the TKE equation (2.1) cannot be negative. In the last hour of day 1,

dissipation exists above the depth of 80 m ($z_{e=0}=80$), with a maximum value of dissipation (e_{max}) of $2.6 \times 10^{-6} \text{ m}^2/\text{sec}^3$ at the 40 m depth. After a near equilibrium state is reached (day 5), dissipation occurs between the surface and the depth of 90 m ($z_{e=0}=90$) with a maximum value of dissipation (e_{max}) of $1.9 \times 10^{-6} \text{ m}^2/\text{sec}^3$ at 40 m. On day 9, dissipation occurs down to the depth of 100 m with a maximum dissipation value of $1.9 \times 10^{-6} \text{ m}^2/\text{sec}^3$ at the region between 40 to 70 m depth. On day 11, $z_{e=0}$ equals 105 m and $e_{max}=1.6 \times 10^{-6} \text{ m}^2/\text{sec}^3$ in the layer of 30-70 m. The greatest magnitude for the momentum flux ($\overline{u'w'}_{max}$) occurs at about 20 m depth every day. The profiles also show that although the depth range of dissipation gets deeper with time, it never exceeds 105 m (above EUC core) in this case.

The shape of the EUC core has been modified by the downward momentum flux. On day 1, there was a rounded EUC core with a jet velocity \overline{u}_{max} equal to 1.4 m/sec at the depth of 100 m. In the period of day 7 to day 9, a narrower EUC jet with a \overline{u}_{max} equal to 1.55 m/sec at the depth of 105 m was formed. On day 11, the location of \overline{u}_{max} has moved down to a 110 m depth again and reaches a value of 1.6 m/sec. The bihourly profiles on the final day (Figure 5), show that the dissipation clears from 10:00 a.m. to 4:00 p.m. During this period the temperature profiles also show the shallowing processes that allow the temperature in the upper 20 m to increase from 24.0°C to 24.25°C. Although the velocity profile changed a little in the first 11 days, both the shape and the maximum velocity value

of the EUC jet remain the same in the bihourly profiles of the final day. This suggests that the EUC jet may be effected by the vertical mixing of the momentum input by the surface wind stress. However, the EUC jet was not effected by the solar diurnal cycle.

As seen in Figure 6, the dissipation diurnal cycle is well defined, even on the first day. After day 5, when an equilibrium state is reached, the phase shift of dissipation with time and depth is clearly seen, as mentioned by Garwood (1990). The innermost closed dissipation contour line occurring in the nighttime is an elongated area which shows the largest dissipation region sinking with time. Also, maximum dissipation is shown to occur at about midnight. The zero dissipation period is caused by strong noontime downward heating (buoyant damping) which balances the mechanical instability induced by momentum transport. This happened on day 1 from 9:00 a.m. to 1:00 p.m., but in day 4 it occurred from 9:00 a.m. to 3:00 p.m. and in day 12 was from 9:00 a.m. to 4:00 p.m. The longer period with no dissipation on later days may be due to adjustment by the model to reach a true equilibrium state. Since the atmospheric forcing was identical each day, the differences in dissipation rates may be attributed to the lack of a true equilibrium state on day 5. After day 5 the daily variation in dissipation is not very significant; therefore, near equilibrium state was assumed at day 5. The vertical integration of dissipation (Figure 7d)

also suggests that equilibrium state is almost achieved by day 5.

The vertical integration of dissipation is influenced strongly by the diurnal cycle of solar radiation. The maximum integral value for each day occurs just before midnight (hour 24). This value slowly decreases until sunrise when it declines sharply to zero at about 10:00 a.m. Two hours before sunset the vertically integrated dissipation value begins to increase. Then at the time of sunset, it increases steeply to a maximum value at about midnight. As shown in Figure 7d, there are minor but unexpected fluctuations in the vertical integral of dissipation for day 4 and day 9 that were initially attributed to numerical instability. However, when the Adamec *et al.* (1981) mixing iteration process was doubled in the number of iterations, the fluctuation remained. These fluctuations remain unexplained.

B. CASE 2

In this case, an arbitrary wind condition was applied to test the effect of increasing or decreasing wind stress to the dissipation. For the first four days, the wind speed (\bar{u}_{10}) was held constant at 6 m/sec to reach an equilibrium state similar to case 1. From day 5 to day 8 the wind speed was linearly increased to 10.8 m/sec, and then it was linearly decreased to 1.1 m/sec for the period from day 9 to day 12 (Figure 8). The

squared friction velocity (u_*^2) was calculated by the equation:

$$u_*^2 = \frac{\rho_a}{\rho_w} C_D \bar{u}_{10}^2 \quad (3.1)$$

Where the air density ρ_a is 1.25 kg/m³, the sea water density ρ_w is 1025 kg/m³, and the drag coefficient C_D is 1.3×10^{-3} . The value of wind stress $\rho_w u_*^2$ for the first four days is about 5.6×10^{-2} N/m², slightly greater than the value in case 1. The vertical integral of dissipation shows the maximum value of each day was correlated with the wind speed. The reason for the fluctuations which occurred on days 3, 4, 5, and 8 are still not understood.

The vertical profiles of \bar{T} , \bar{u} , $-\overline{u'w'}$, and ϵ for the first four days are almost identical to those for case 1 (Figure 9). The most interesting results occurred during the periods when the wind speed was varied. Therefore, the bihourly profiles for day 8 and day 9 are plotted in Figure 10 and 11 to show the effect of variable wind forcing on the daily cycle.

In the day 5 profiles shown in Figure 9, the greatest magnitude for the momentum flux occurred at 20 m, increasing to a value of 10×10^{-5} m²/sec² with the downward momentum flux extending to a depth of 100 m. The maximum dissipation (ϵ_{max}) increased to 2.5 m²/sec³ at a depth of 50 m. Those results are different from those in case 1, showing that increasing the wind forcing can produce a larger downward transport of energy that reaches to a greater depth. The shape of the EUC core

narrowed at day 7 and the \bar{u}_{\max} location occurred at 110 m depth, earlier and deeper than that in case 1. Table I summarizes values of $\overline{u'w'}_{\max}$, ϵ_{\max} , their respective depths, and depth at which dissipation and momentum flux vanishes ($z_{\epsilon=0}$). From this table, a comparison of $\overline{u'w'}_{\max}$ with the wind speed (\bar{u}_{10}) shows that the value of $\overline{u'w'}$ at 20 m depth is proportional to the wind speed. At day 10 hour 24, $u_{10}=6.0$ m/sec again and the $\overline{u'w'}_{\max} = -8 \times 10^{-5} \text{ m}^2/\text{sec}^2$, the same value as in the first four days. Since wind speed is decreasing at this time, this result suggests there is no time lag for $\overline{u'w'}$ flux to reach the depth of 20 m. Maximum dissipation value increases corresponding to increasing of $\overline{u'w'}_{\max}$ in depth of 20 m. Likewise, the depth of maximum dissipation ($z_{\epsilon=\max}$) increased during the period between day 5 and day 8. However, the maximum depth of dissipation ($z_{\epsilon=0}$) continually deepened with time to reach 115 m at day 10 then subsequently shallowed due to lack of mechanical energy (weak wind stress) input.

From the bihourly profiles for day 8 (Figure 10), the downward displacement of the location of \bar{u}_{\max} can be clearly observed. During the maximum solar heating period of a day (hour 10 to hour 16) when the dissipation vanished in case 1, the dissipation was still evident in case 2 with a minimum value of $1.3 \times 10^{-6} \text{ m}^2/\text{sec}^3$ at 11:00 a.m. at a depth of 20 m. This occurred because the buoyant damping did not balance the increased shear production of turbulence due to a stronger wind stress. The bihourly profiles for day 9 (Figure 11) show

TABLE 1. DAILY INFORMATION ON WIND SPEED (\bar{u}_{10}), MAXIMUM VALUE OF DOWNWARD MOMENTUM FLUX , MAXIMUM VALUE OF DISSIPATION RATE (e_{10}), DEPTH OF MAXIMUM DISSIPATION ($z_{e=\max}$), DEPTH RANGE OF DISSIPATION ($z_{e=0}$), AND DEPTH OF EUC JET ($z_{\bar{u}=\max}$) BASED ON PROFILES OF CASE 2.

	\bar{u}_{10} (m/s)	$\overline{u'w'}_{\max}$ 10^{-5} (m^2/s^2)	e_{\max} 10^{-6} (m^2/s^3)	$z_{e=\max}$ (m)	$z_{e=0}$ (m)	$z_{\bar{u}=\max}$ (m)
Day 1	6	-8	2.8	35	75	112
Day 2	6	-8	2.4	40	80	112
Day 3	6	-8	2.2	40	90	110
Day 4	6	-8	2.0	40	95	108
Day 5	7.2	-10	2.5	50	100	105
Day 6	8.4	-13	3.0	60	105	110
Day 7	9.6	-16	3.4	70	105	110
Day 8	10.8	-18	3.7	80	110	115
Day 9	8.4	-13	2.4	75	115	117
Day 10	6.0	-8	1.4	40	115	120
Day 11	3.6	-2	0.4	20	25	120
Day 12	1.2	0	0	0	0	120

that the effect of maximum wind stress on the zonal velocity remained for several hours and preserved the shape of a narrowed EUC core. This is consistent with the phase shift of dissipation with time and depth shown in case 1. The bihourly dissipation profiles of the final day (Figure 12) provide more evidence for the downward propagation of momentum to a relatively shallower depth. Dissipation ceases three hours after sunrise due to the low wind stress condition.

Contours of dissipation (Figure 13) are a complete picture of dissipation versus time and depth $e(z,t)$. They show the dissipation value increasing and deepening during the linearly increasing wind period, and decreasing in the period of linearly decreasing wind. The strongest dissipation occurred at late day 8 and early day 9, when the wind stress was also strongest. Two closed contour lines at 40 m depth during noontime of day 8 and early day 9 are relative minimum dissipation values of 8×10^{-7} and $6 \times 10^{-7} \text{ m}^2/\text{sec}^3$ respectively. These two shallow dissipation minima suggest that strong daytime solar shortwave heating has its greatest effect at the depth of 40 m. On day 10 hour 22, there are double maxima in dissipation, at depths of 40 and 70 m. This higher dissipation in the deeper region may be attributable to the phase lag between mechanical energy input at the surface and the vertical-propagation of dissipation "event."

C. CASE 3

In this case, the wind is held constant for seven days to reach equilibrium state. Then the model was forced with stresses computed using speed observed during the Tropic Heat I Experiment. Figure 14 shows the observed wind speed and the calculated value for u_{10} from equation (3.1). The surface heat fluxes were the same as in previous cases. This figure also allows comparison of the vertical integral of dissipation with time series for the atmospheric forcing. The daily cycles are

dominated by the diurnal solar radiation. The value for the vertical integral of dissipation is also influenced strongly by the wind stress. This is consistent with the results for the first two cases.

Profiles of model simulation are again plotted for the last hour of odd number days and every two hours for the final day. Because the wind conditions shown in Figure 14 indicate periods of high wind speed (\bar{u}_{10}), a greater depth of penetration and larger value for dissipation were expected. Figure 15 shows that the depth of dissipation region ($z_{\epsilon=0}$) at day 1 was 100 m and deepened to 145 m at day 11. On day 9, a secondary dissipation maximum was predicted at 110 m near the bottom of the dissipation region. This coincides with increased mixing of heat and momentum in the deeper region. A narrowed EUC core formed on day 3. After day 7, the zonal velocity gradient became greatly negative above the EUC jet and small positive just under the EUC jet. More detailed daily information on $\overline{u'w'}_{\max}$ (maximum downward momentum flux), ϵ_{\max} (maximum dissipation value), $z_{\epsilon=\max}$ (depth of maximum dissipation occurred), $z_{\epsilon=0}$ (depth of dissipation vanished), \bar{u}_{\max} (maximum zonal velocity of EUC), and $z_{\bar{u}=\max}$ (depth of EUC jet speed) has been summarized in Table II.

In Table II, downward extension of the dissipation region and propagation of the EUC core reflected by the downward momentum transport due to wind stress are highlighted once more. The dissipation region ($z_{\epsilon=0}$) and depth of the EUC core

($z_{\bar{u}=\max}$) extended downward at a faster speed than in the previous cases and reached a greater depth. Although the wind stress varied with time, the total dissipation was highly correlated with the downward momentum flux which corresponds to the wind stress. The secondary maximum dissipation regions shown in the table are marked in parentheses. For the last three days, the small secondary dissipation maximum under the EUC core are caused by small upward momentum flux together with a positive zonal velocity gradient, generating turbulent kinetic energy under the EUC core. At day 11 and 12, the depth where dissipation vanishes ($z_{\epsilon=0}$) lies below the depth of the EUC jet ($z_{\bar{u}=\max}$) because of the upward momentum flux under the EUC core.

Figure 16 illustrates the diurnal cycle of the final day. Dissipation weakened between hour 10 and hour 16 when the solar radiation is strong. This is consistent with the previous results. The zonal velocity profile did not change between hourly observations. Also, $\bar{u}(z)$ increased nearly exponentially from the surface to the depth of the jet then slowly decreased for about 20 m below the jet. The deep profile of zonal velocity remains unchanged. For all 12 plots in this figure, there is a small local dissipation maximum between the depths of 135 m to 145 m with the maximum value occurring right at the jet level. The value of shear production, $(-\overline{u'w'} \frac{\partial \bar{u}}{\partial z})$, must always be positive, so the small positive zonal velocity gradient below the EUC jet together

TABLE II. DAILY INFORMATION BASED ON CASE 3. SOME SECONDARY MAXIMUM DISSIPATION VALUES ARE LISTED IN PARENTHESIS.

	$\overline{u'w'}_{\max}$ 10^{-5} (m^2/s^2)	e_{\max} 10^{-6} (m^2/s^3)	$z_{\epsilon=\max}$ (m)	$z_{\epsilon=0}$ (m)	\bar{u}_{\max} (m/s)	$z_{\bar{u}=\max}$ (m)
Day 1	-11	2.7	55	100	1.6	105
Day 2	-11.5	2.6	60	105	1.6	110
Day 3	-13	2.9	65	105	1.75	110
Day 4	-18	3.7	70	110	1.5	115
Day 5	-16	3.2	80	115	1.55	120
Day 6	-13	2.1	70	115	1.45	120
Day 7	-14	2.4	95	115	1.48	120
Day 8	-16	2.5 (2.1)	90 (115)	120	1.5	125
Day 9	-15	2.3 (2.1)	80 (110)	120	1.4	125
Day 10	-20	3.2 (0.2)	105 (125)	130	1.4	130
Day 11	-15	2.5 (0.3)	100 (135)	145	1.35	135
Day 12	-14	2.3 (0.3)	95 (140)	145	1.4	140

with small upward momentum flux can generate TKE to give a secondary but weaker dissipation region under the core.

The time series of dissipation (Figure 17) reflects the wind stress effects. On day 1 hour 11, a peak in dissipation was caused by a wind speed maximum just before noon as shown in Figure 14. On days 2, 3, 4, 5, 7, 9, and 12, there are two local dissipation maxima at early morning. These are also attributable to the wind fluctuation history. Based on this figure, Table III summarizes the time (day and hour) and value

of maximum (or minimum) dissipation (ϵ_{\max}), depth of the maximum (or minimum) dissipation ($z_{\epsilon=\max}$), wind velocity at that instance (\bar{u}_{10}), and the status of the wind. Here, the geometric center of the innermost closed contour line is used to compute the maximum (or minimum) value.

The table indicates that the maximum dissipation values occurring in the early morning (before 6:00 a.m.) always corresponded to peaks in wind speed. However, in the nighttime the maximum dissipation values did not always correspond to the wind fluctuations. Sometimes the dissipation maximum lagged the fluctuation by one or two hours. The minimum values of dissipation always occurred in the daytime (between hour 10 and 14) and corresponded to wind minima.

TABLE III. A LISTING OF MAXIMUM (MINIMUM) DISSIPATION RATE, ITS DEPTH, AND WIND SPEED BASED ON DISSIPATION CONTOURS OF CASE 3.

Day	Hour	ϵ_{\max} ($10^{-6} \text{ m}^2 \text{ s}^{-3}$)	$z_{\epsilon=\max}$ (m)	\bar{u}_{10} (m s ⁻¹)	status of \bar{u}_{10} (numbers are in units of m sec ⁻¹)
1	11	0.4	20	7.54	maximum value of a narrow spike
1	20	2.6	25	7.26	decreasing, 2 hrs. after maximum value of 7.39
1	23	2.6	55	7.56	maximum value
2	6	2.0	60	7.02	increasing, 3 hrs. after minimum value of 6.19, 1 hr. before maximum value of 7.22
2	24	2.4	60	7.56	maximum value
3	6	2.4	65	7.64	maximum value
3	20	3.4	65	8.93	decreasing, 1 hr. after maximum value of 9.30
4	4	2.8	70	9.12	maximum value
4	24	3.8	75	10.55	maximum value

Day	Hour	ϵ_{\max} ($10^{-6} \text{ m}^2/\text{s}^3$)	$z_{\epsilon=\max}$ (m)	\bar{u}_{10} (m/s)	status of \bar{u}_{10} (numbers are in units of m/sec)
5	4	4.0	75	11.14	maximum value
5	13	(ϵ_{\min}) 0.8	45	10.10	minimum value. 3 hrs. after maximum value of 11.10. 2 hrs. before next maximum value of 10.65
5	20	3.4	80	9.78	decreasing. 2 hrs. after maximum value of 10.55
6	2	3.6	75	11.10	maximum value
6	10	(ϵ_{\min}) 0.2	40	9.23	increasing. 2 hrs. after minimum value of 8.72. before maximum value of
6	20	2.6	75	8.90	decreasing. 2 hrs. after maximum value of 9.37
7	1	2.2	70	8.82	maximum value
7	6	2.2	80	8.98	increasing. 3 hrs. after minimum value of 8.56. 4 hrs. before maximum value of 9.86
7	21	2.8	95	9.69	decreasing. 1 hr. after maximum value of 9.89
8	1	2.6	90	9.73	maximum value
8	20	(ϵ_{\min}) 1.8	25	7.65	minimum value. 1 hr. after maximum value of 7.76. 3 hrs. before next maximum value of 9.02
8	24	2.6	85	8.48	decreasing. 1 hr. after maximum value of 9.02
9	6	2.0	80	8.97	maximum value
9	20	2.6	25	9.11	decreasing. 1 hr. after maximum value of 9.22
9	24	2.4	80	9.17	maximum value
10	20	2.8	40	10.30	maximum value
10	24	3.2	110	10.90	decreasing. 1 hr. after maximum value of 10.94
11	20	2.4	30	9.31	decreasing. 1 hr. after maximum value of 9.37
11	22	2.6	100	9.46	maximum value
12	6	2.4	95	9.89	maximum value

Day	Hour	ϵ_{\max} ($10^{-6} \text{ m}^2 \text{ s}^3$)	z_{\max} (m)	\bar{u}_{10} (m s)	status of \bar{u}_{10} (numbers are in units of m/sec)
12	20	2.4	40	9.65	decreasing, 1 hr. after maximum value of 9.67
12	223	2.8	95	9.35	decreasing, 1 hr. after maximum value of 9.67

D. CASE 4

For the last case the wind speed is held constant for seven days until a near equilibrium state is achieved. Then the model is forced with observed wind and observed solar radiation data. Comparing the result in this case with the result in case 3 can give some understanding of the physical effect of solar radiation on dissipation. For this case, a comparison was made between the model prediction and actual observations, this case is the best test of the model. Atmospheric forcing was the same as in case 3 (Figure 18). Solar radiation recorded in the Tropic Heat I Experiment is higher than the value used in previous cases. Here the maximum radiation reached values of $1,000 \text{ W/m}^2$. An average value for back longwave radiation of 150 W/m^2 was assumed. This resulted in the heat nighttime net heat loss of 150 W/m^2 and daytime heat gains sometimes reaching 850 W/m^2 at midday.

Because the atmospheric forcing in the nighttime is identical to that of case 3, the trend of vertical integral of dissipation has a shape similar in Figure 18 to that in Figure 14. However, the integrated dissipation values in the daytime

are somewhat less in this case due to stronger shortwave heating, and the integrated dissipation values are slightly larger in the nighttime. The lower value of the integral of dissipation in the daytime and larger value at the nighttime is explained as follows. Because of the larger solar heating during the day in this case, there is a shallower daytime mixed layer. For the same wind stress applied to the sea surface, a larger mean kinetic energy is expected to exist in the shallower mixed layer, based on conservation of momentum. In the nighttime, shear production, which is a conversion of mean KE to TKE is not balanced by buoyant damping. The downward momentum flux will act with the mean shear to convert more KE into TKE, and this will be reflected by the increased dissipation rate. Therefore, the maximum in dissipation at day 1 hour 11 which was caused by a wind maximum in case 3 is not evident in this case. There are three daytime events with fluctuations in integrated dissipation: at the midday of day 3 and before noon on days 7 and 12. These events are attributed to stronger wind, coincident with a reduction in solar heating due to cloud cover, shown in Figure 18b and 18c.

The bidaily profiles shown in Figure 19 are almost identical to those obtained for case 3. The shape of the profiles of dissipation, the maximum vertical extent of dissipation ($z_{t=0}$), and the zonal velocity changes are very similar to Figure 15. Only a slightly higher nighttime dissipation rate is reached after day 5, and a larger upward

momentum flux under the EUC core is found in day 11. That means higher solar heating in the daytime cannot change the downward entrainment velocity. However, it may make small contributions to the TKE budget.

The bihourly profiles for the last day (Figure 20) show that before hour 8, the vertical distribution of dissipation is similar in cases 3 and 4 with a slightly larger rate in the latter. At hour 10, the profiles in case 3 and in case 4 are virtually identical. During the period of high solar heating (hour 11 to 14) the net dissipation in case 4 is greatly decreased. From then until hour 18, dissipation in case 4 is strong at 20 m but weaker in the lower depths. The hour 20 profile shows that the dissipation rate for case 4 reaches its maximum value at a depth of 35 m, the value much larger than that in the same time at the same depth in case 3, and it approaches the same value of case 3 at 100 m. Table IV lists the dissipation values at three different depths in cases 3 and 4 to demonstrate this effect.

A comparison of the contours of dissipation in case 4 (Figure 21) to those of case 3 dissipation at the 40 m depth almost every local noontime. The only exception was on day 8, when Figure 21 shows a $0.2 \text{ m}^2/\text{sec}^3$ dissipation contour starting at hour 11, and corresponds to the cloud cover increase at that time. In the first three days, the nighttime dissipation maximum are almost the same value and depth but covered a larger region and longer duration (Figure 21). After early

TABLE IV. LISTING OF DISSIPATION AT THREE DIFFERENT DEPTHS IN CASES 3 AND 4

Day 12 hour	Case 3 e_z (10^{-6} m ² /sec ³)			Case 4 e_z (10^{-6} m ² /sec ³)		
	z=100	z=50	z=20	z=100	z=50	z=20
2	2.6	1.9	0.9	2.6	2.0	1.0
4	2.3	1.6	0.7	2.3	1.7	0.8
6	2.3	1.5	0.7	2.3	1.6	0.7
8	2.1	1.4	0.8	2.2	1.5	0.9
10	0.7	0.4	0.7	0.7	0.4	0.7
12	0.4	0.3	1.0	0.2	0.1	0.5
14	0.3	0.3	1.2	0.1	0.1	1.2
16	0.4	0.3	1.5	0.1	0.2	1.6
18	1.3	1.1	2.1	1.0	0.9	2.5
20	2.8	2.3	1.9	2.8	2.5	2.2
22	2.8	2.3	1.4	2.9	2.6	1.6
24	2.4	2.0	1.0	2.5	2.2	1.2

morning (hour 4) of day 4, the maxima of dissipation at 70 m in case 4 are generally larger than those maxima in case 3 by one contour increment, a value of 2×10^{-7} m²/sec³. A significant dissipation increase in case 4 is noted at 40 m depth between hour 18 to 20 of each day. The maximum of dissipation in case 4 increased by 4×10^{-7} m²/sec³ or more than those in case 3. This event shows that right after sunset the increased upward buoyancy flux due to daytime sea surface heating will tend to destabilize the fluid more in shallow regions than in deeper regions.

E. COMPARISON AND SUMMARY

Observed depth-averaged dissipation for the Tropical Heat I Experiment are shown in Figure 22 (Moum and Caldwell, 1985). In this figure, Moum and Caldwell showed that the major variation in turbulent mixing (ϵ) was associated with daily changes in the sign of the surface buoyancy flux. It is also noted by Moum et al. (1989) that dissipation differed by nearly a factor of 10, on average, between local noon and early morning, increasing through the night and decreasing suddenly several hours after sunrise (Figure 23). Daytime profiles show decreases in dissipation of more than a factor of 100 from profiles during the night. Table V comes from averaging the vertical dissipation integral of each hour in case 4. The results of this calculation compare favorably with the observations of dissipation, showing differences in $\int \epsilon dz$ by a factor of 10 between local noon and early morning. For all four model runs, the dissipation diurnal cycle is dominated by the diurnally changing buoyancy flux, as concluded by Moum and Caldwell (1985). The dissipation results also show that dissipation increases approximately two hours before sunset and reaches a daily maximum at about hour 22 local time. Dissipation then decreases about two hours after sunrise and reaches a daily minimum at about local noon. This is also in agreement with the observations.

TABLE V. AVERAGED VERTICAL INTEGRAL OF DISSIPATION FOR EACH HOUR IN CASE 4

Hour	Integrated averaged dissipation ($10^{-4} \text{ m}^3/\text{sec}^3$)	Hour	Integrated averaged dissipation ($10^{-4} \text{ m}^3/\text{sec}^3$)
1	0.4311	13	0.0276
2	0.4177	14	0.0441
3	0.4001	15	0.1410
4	0.3892	16	0.0836
5	0.3810	17	0.1565
6	0.3795	18	0.2370
7	0.3779	19	0.3045
8	0.3374	20	0.4279
9	0.2362	21	0.4555
10	0.1423	22	0.4612
11	0.1380	23	0.4594
12	0.0411	24	0.4088

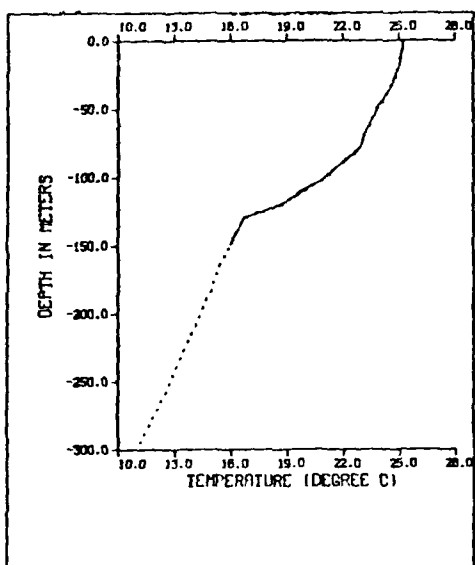


Figure 1. Typical equatorial temperature profile observed at 140°W. Dotted portion under 150m depth is artificial and not relevant to this study.

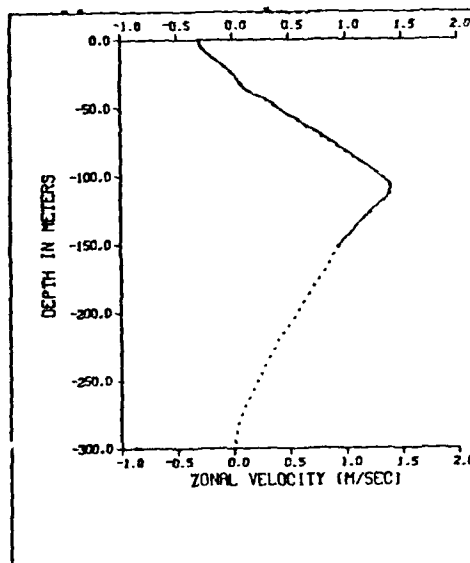


Figure 2. Typical zonal velocity profile on equator observed at 140 W. Dotted portion under 150m depth is artificial and not relevant to this study.

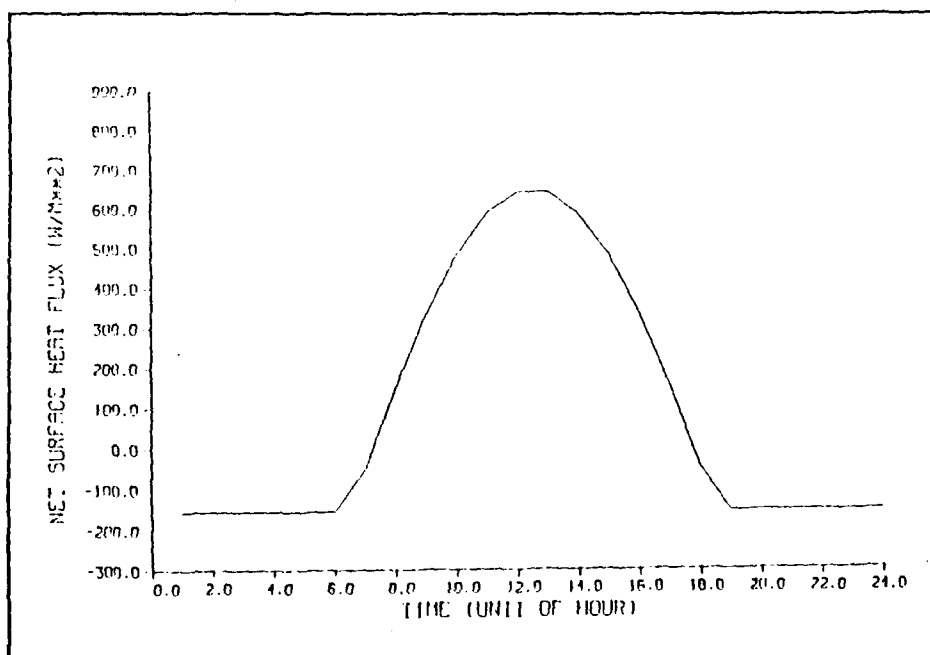


Figure 3. Net downward surface heat flux for prescribed first three cases.

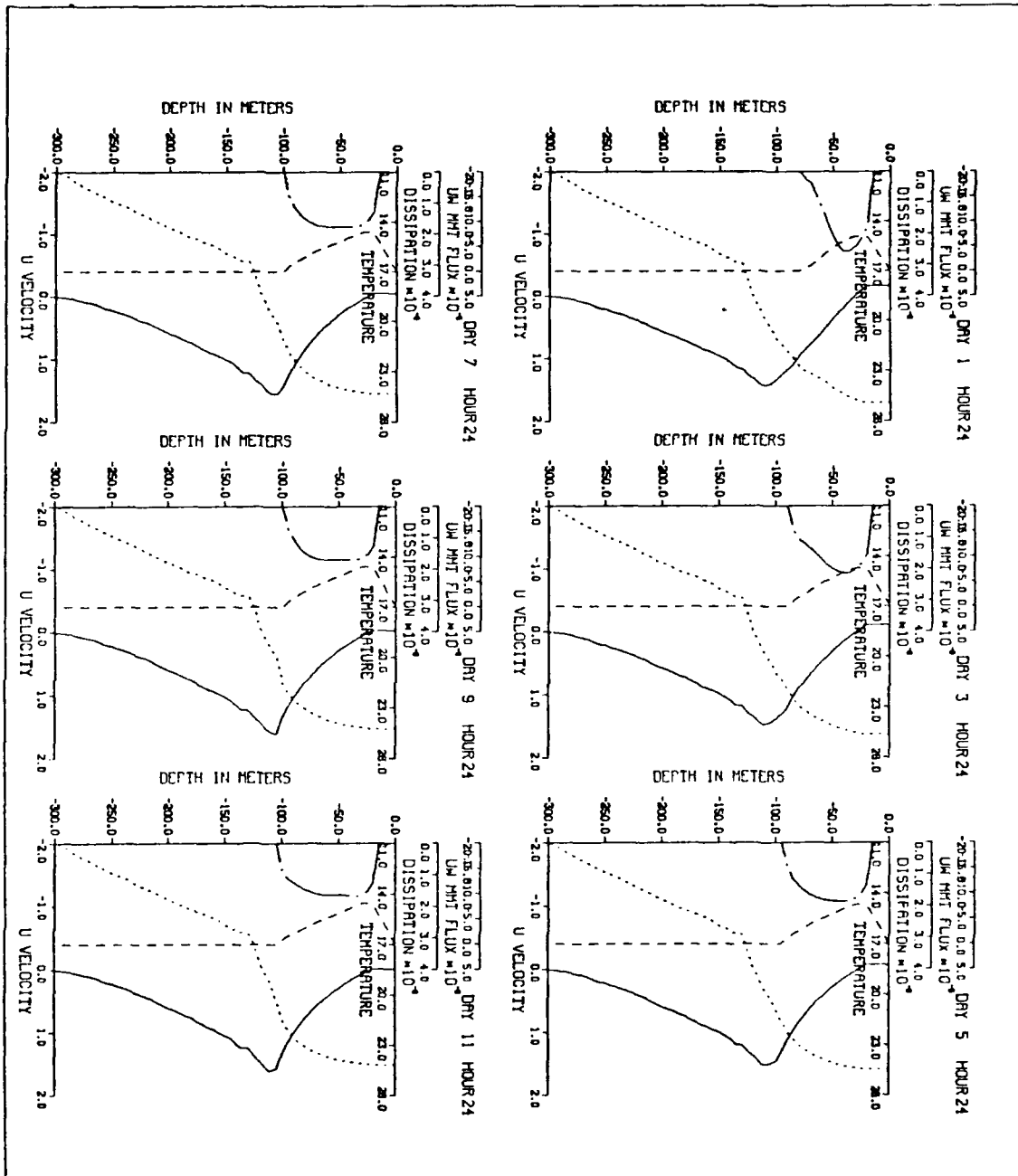


Figure 4. Bidaily model-predicted profiles of zonal velocity ($\bar{u}(z)$ solid line m/sec), temperature ($\bar{T}(z)$ dotted line degree C), downward momentum flux ($-\bar{u}'w'$ (z) dashed line m^2/sec^2), and dissipation ($\epsilon(z)$ chain-dot line m^2/sec^3) for case 1.

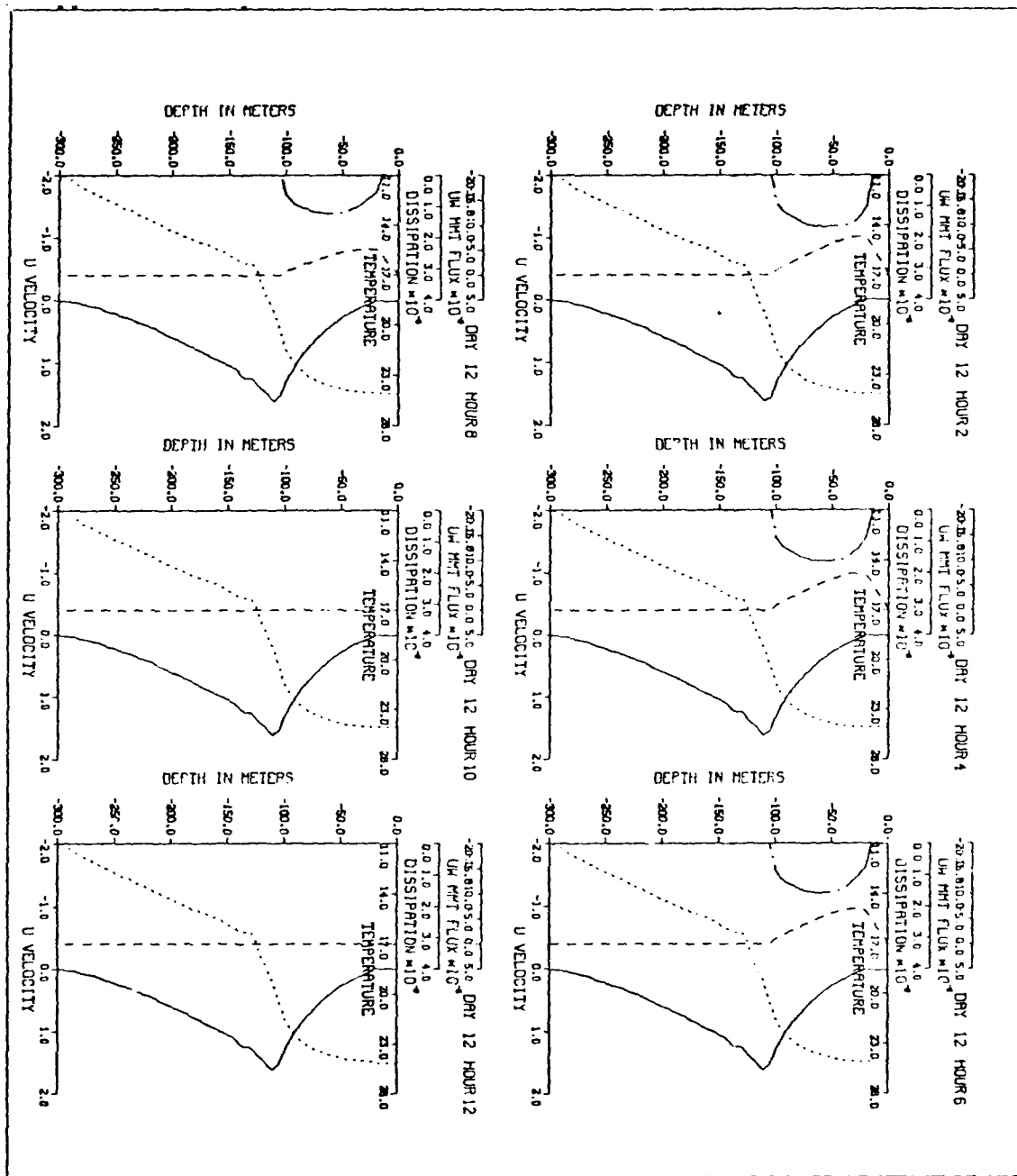


Figure 5. Bihourly model-predicted profiles of zonal velocity ($\bar{u}(z)$ solid line m/sec), temperature ($\bar{T}(z)$ dotted line degree C), downward momentum flux ($-\bar{u}'w'(z)$ dashed line m^2/sec^2), and dissipation ($e(z)$ chain-dot line m^2/sec^3) for day 12 of case 1.

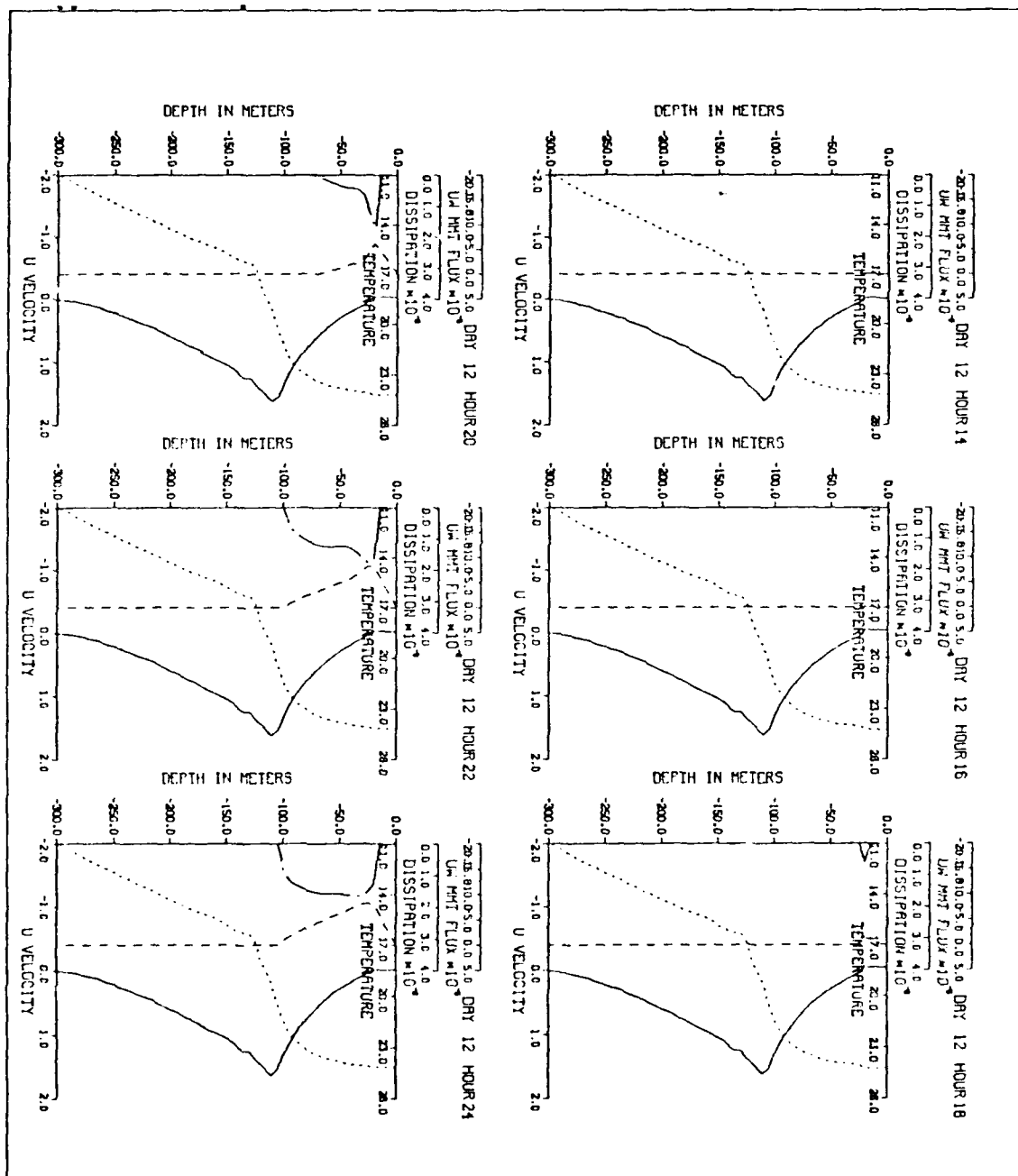


Figure 5 continued

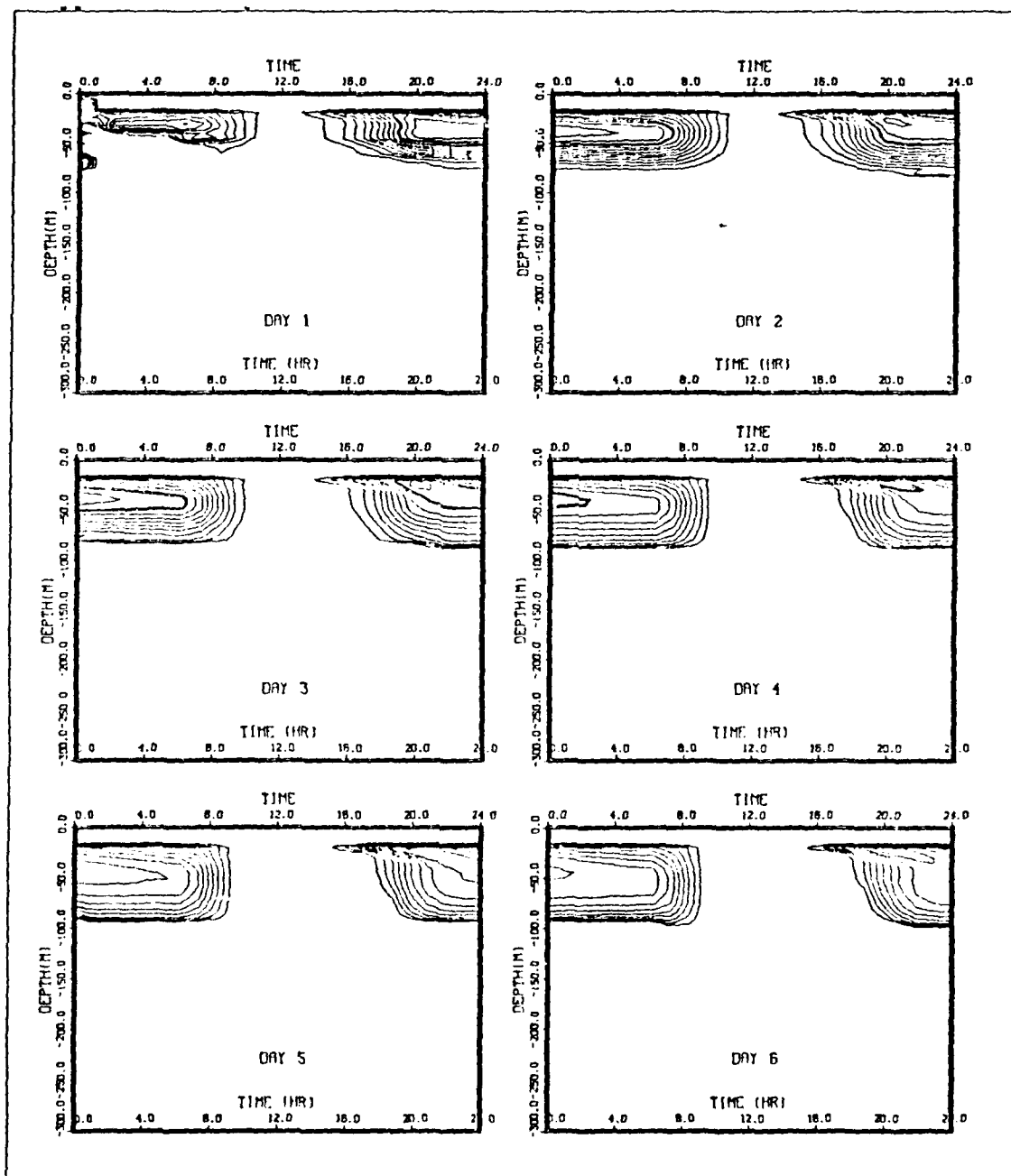


Figure 6. Predicted vs. t and z daily dissipation for case 1. The contour increment is $2 \times 10^{-7} \text{ m}^2/\text{sec}^3$.

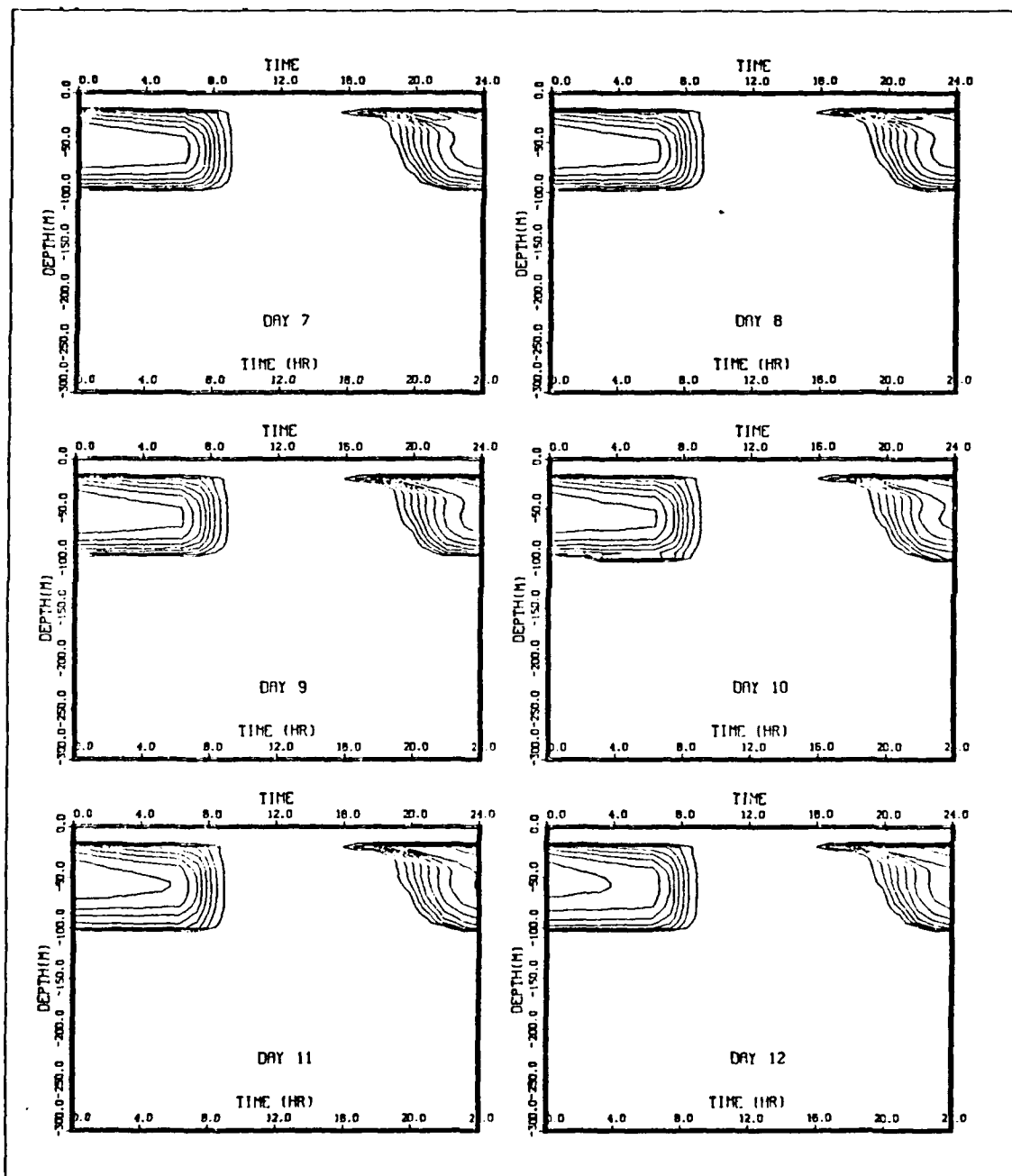


Figure 6 continued

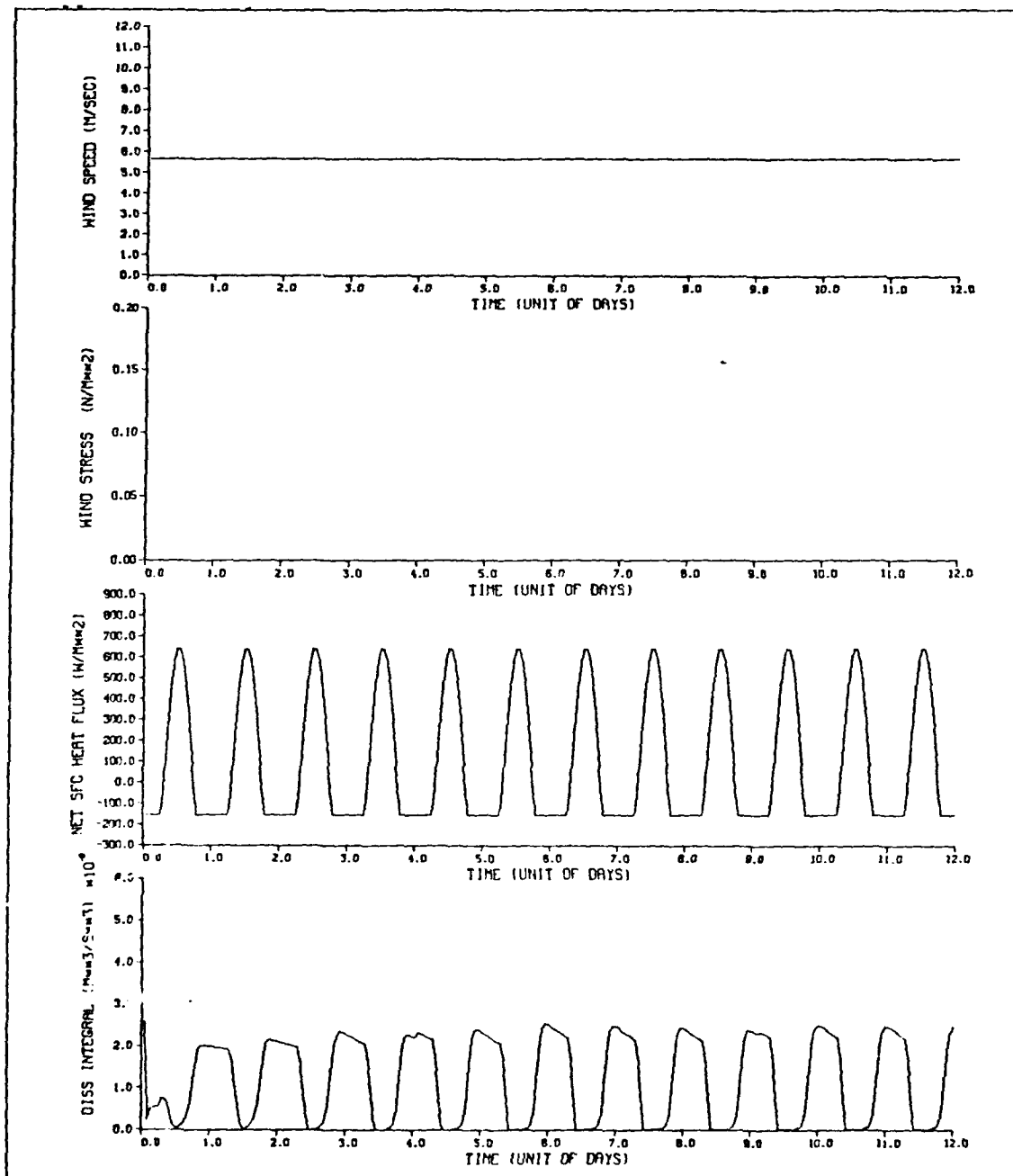


Figure 7. Surface forcing conditions and vertical integral of dissipation for case 1. (a) Constant wind speed of $\bar{U}_{10} = 5.7$ m/sec is shown. (b) Wind stress is constant value of 0.05 N/m^2 . (c) Sum of simulated solar radiation and backradiation is periodically cycled every day. (d) Vertical integral of dissipation shows a clearly diurnal dissipation cycle.

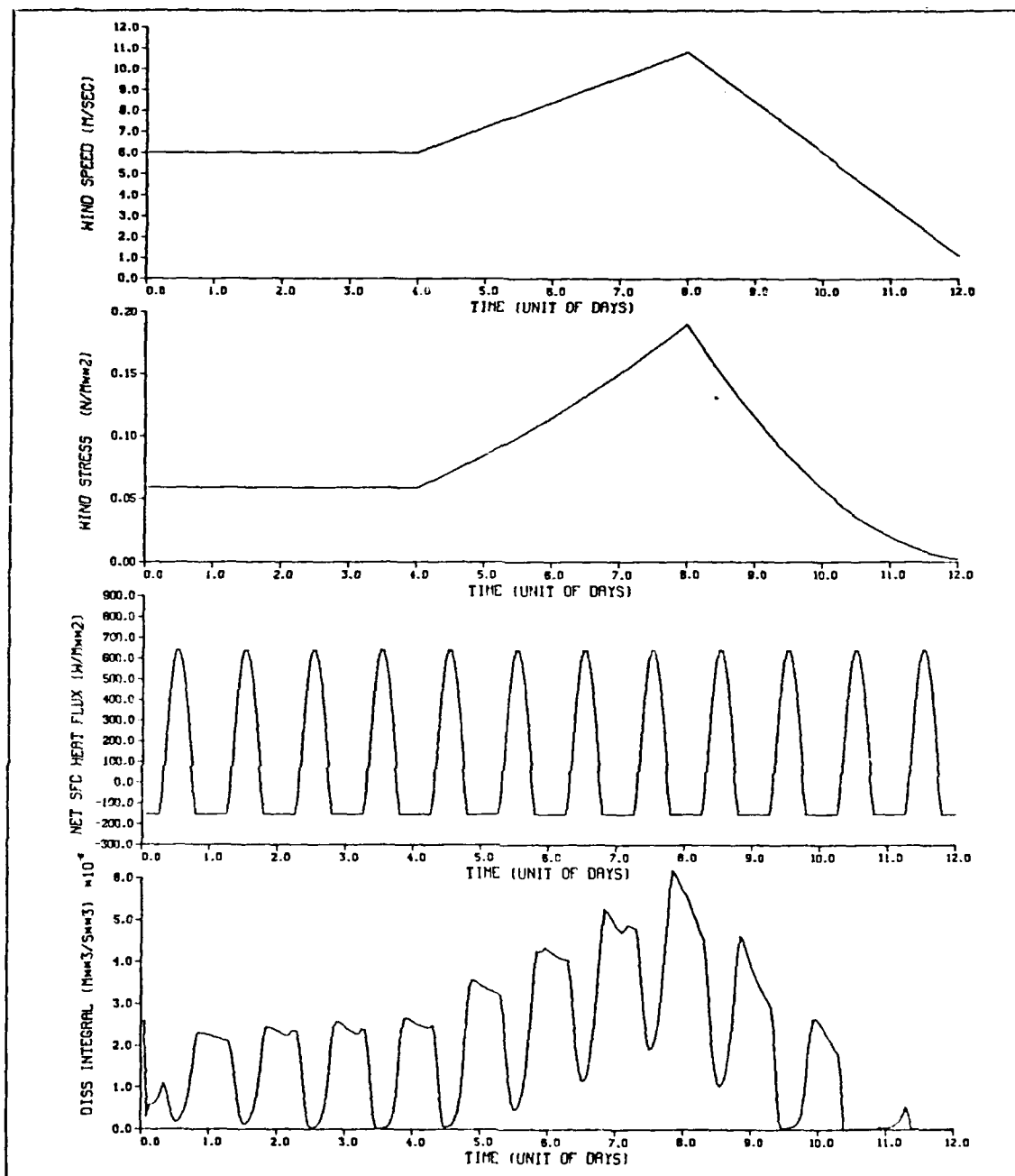


Figure 8. Surface forcing conditions and vertical integral of dissipation for case 2. (a) Wind speed is held constant value of 6 m/sec for 4 days. From day 5 to day 8, the wind speed is linearly increased to 10.8 m/sec then it is linearly decreased to 1.1 m/sec for the period from day 9 to day 12. (b) The wind stress calculated from equation 3-1. (c) Net surface heat flux is the same as in case 1. (d) Vertical integral of dissipation.

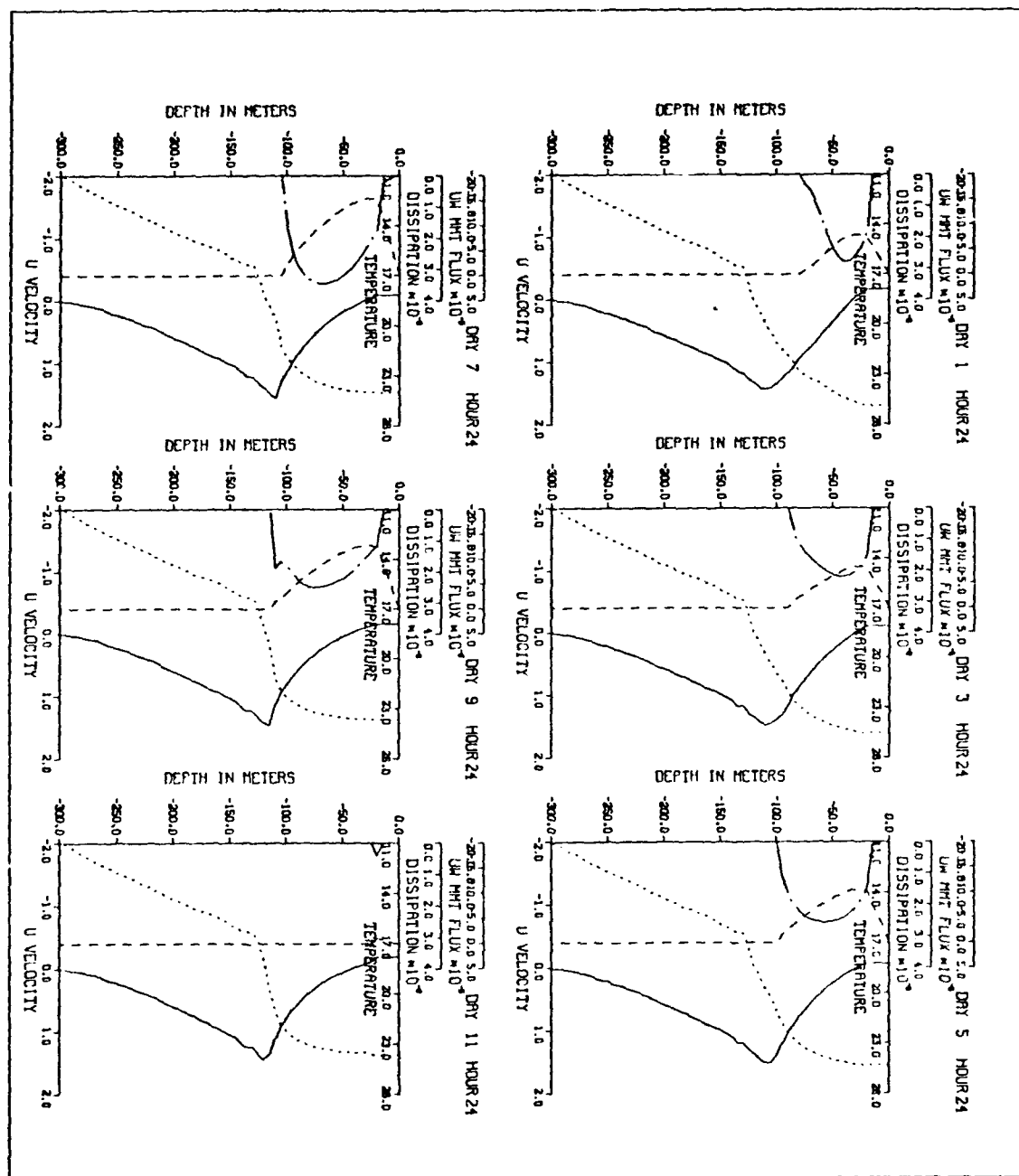


Figure 9. Bidaily model-predicted profiles of zonal velocity ($\bar{u}(z)$ solid line m/sec), temperature ($\bar{T}(z)$ dotted line degree C), downward momentum flux ($-\bar{u}'w'(z)$ dashed line m^2/sec^2), and dissipation ($\epsilon(z)$ chaindot line m^2/sec^3) for case 2.

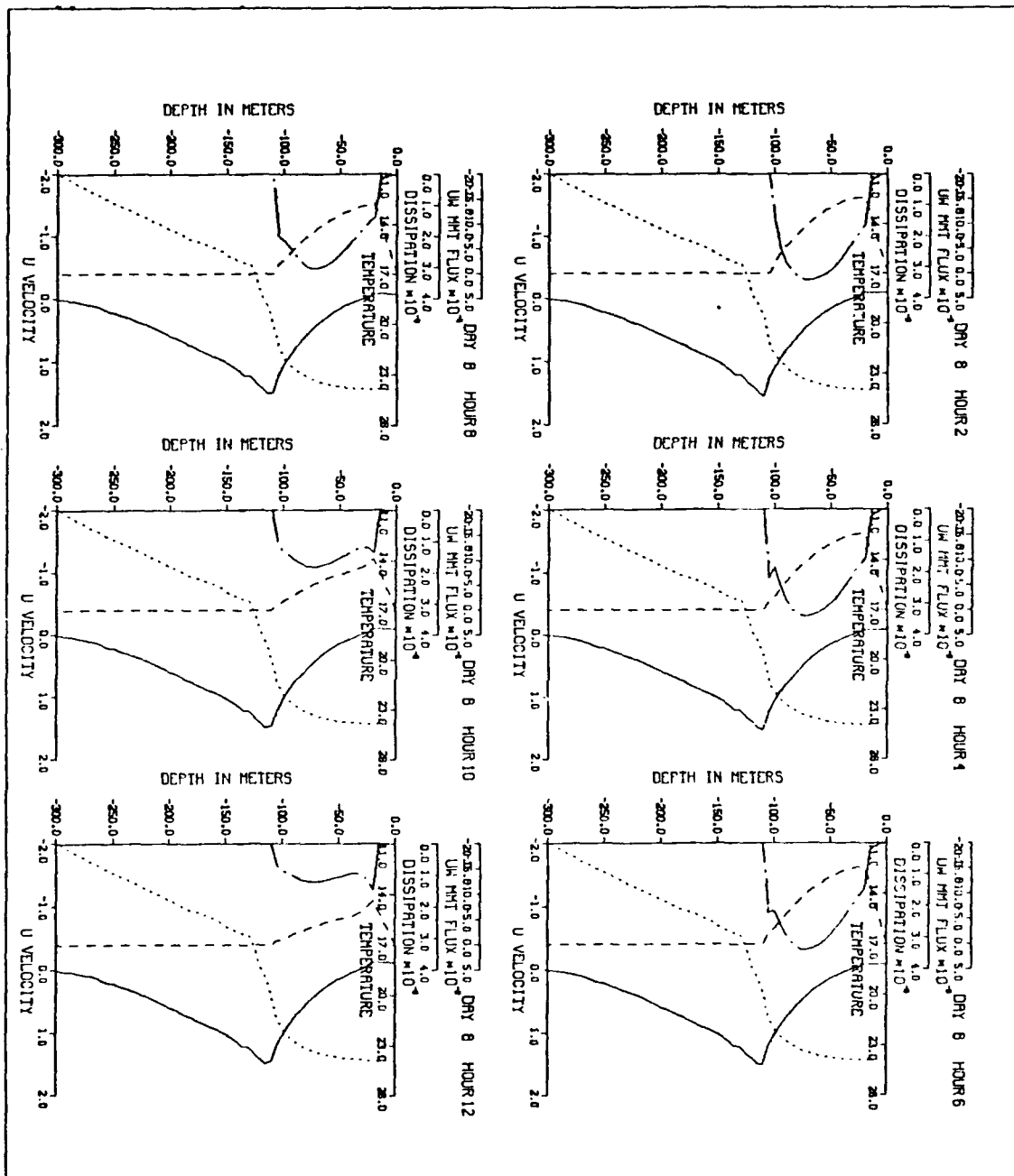


Figure 10. Bihourly model-predicted profiles of zonal velocity ($\bar{u}(z)$ solid line m/sec), temperature ($\bar{T}(z)$ dotted line degree C), downward momentum flux ($-\bar{u}'w'$ (z) dashed line m^2/sec^2), and dissipation ($\epsilon(z)$ chain-dot line m^2/sec^3) for day 8 of case 2.

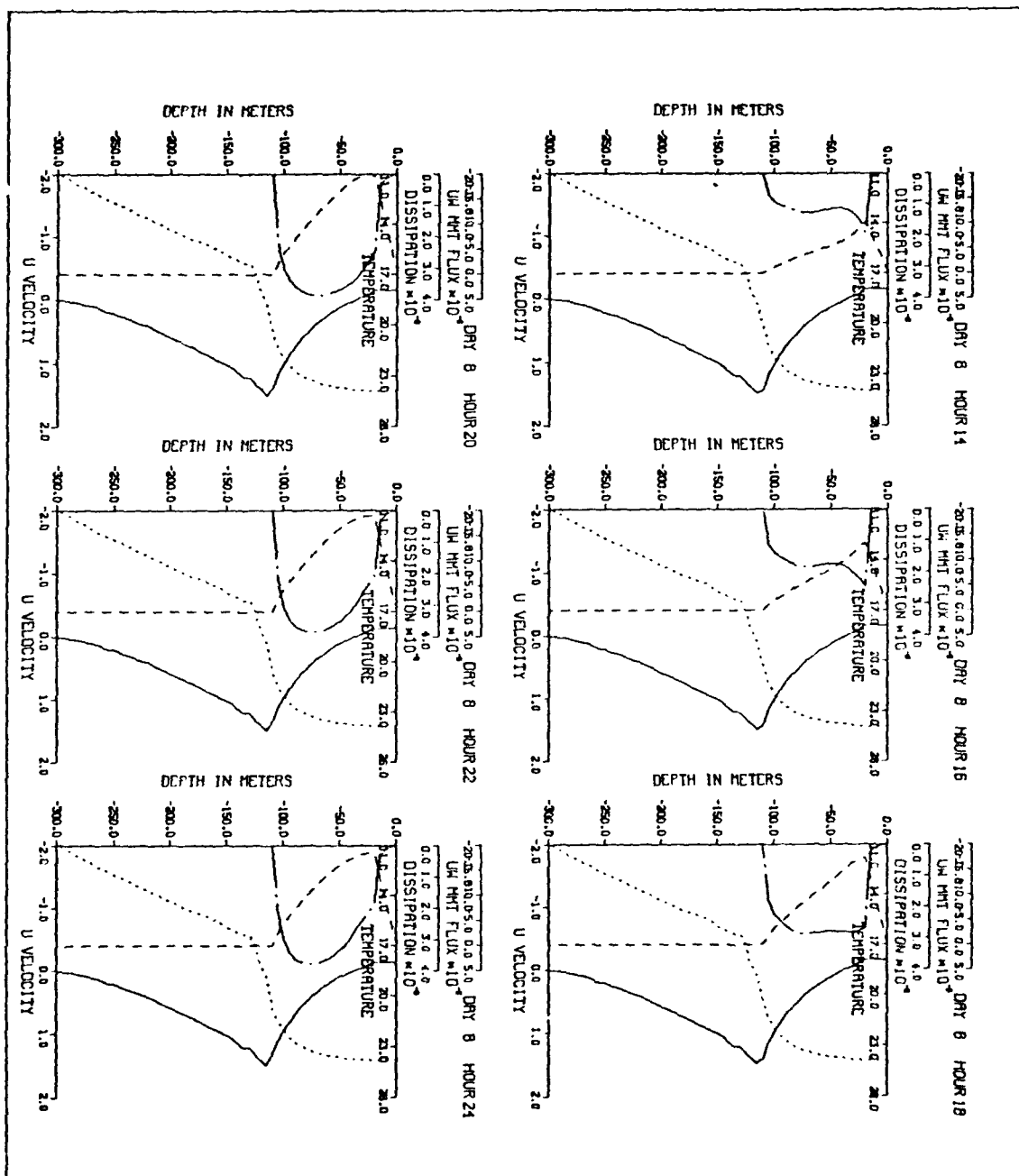


Figure 10 continued

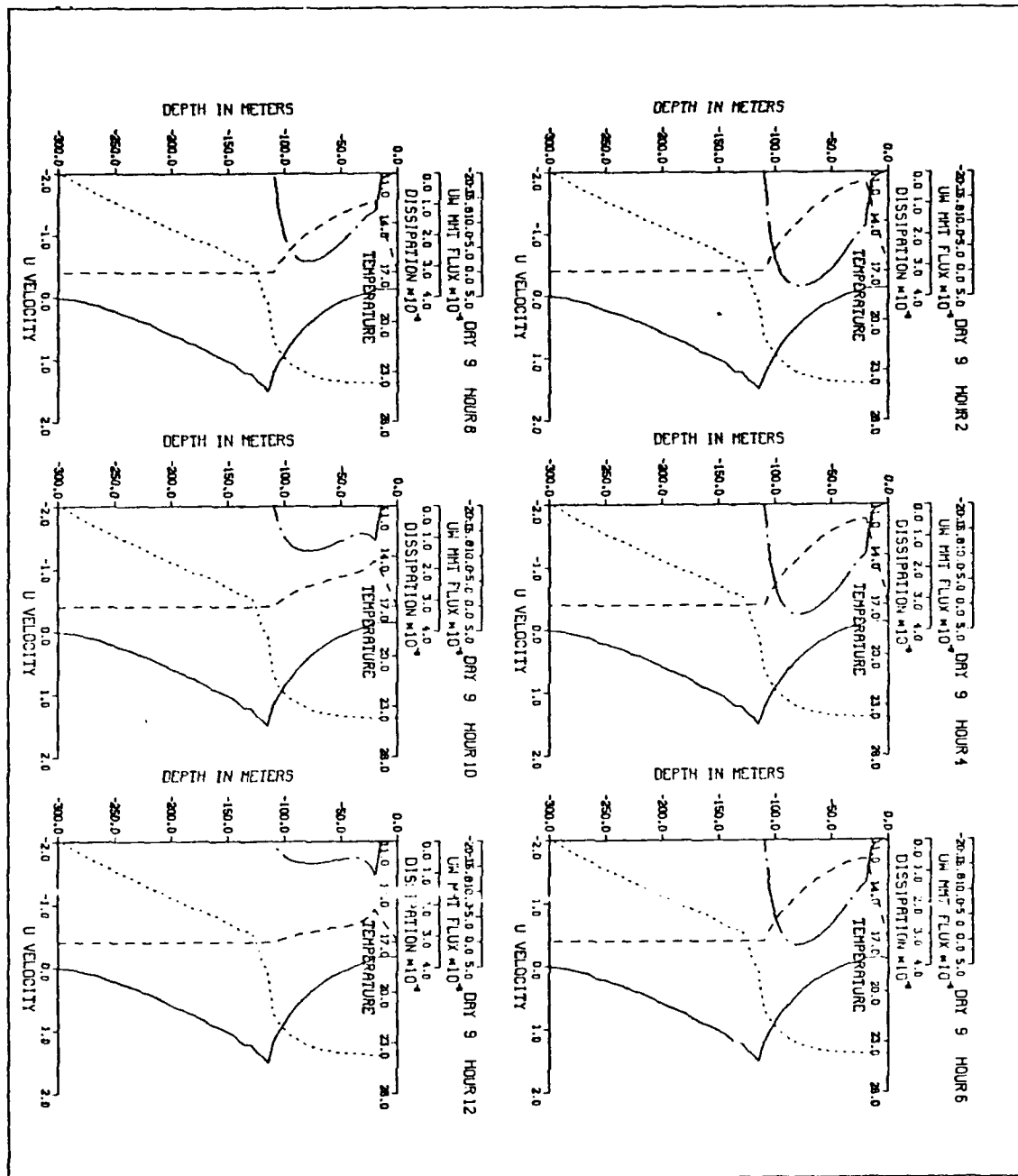
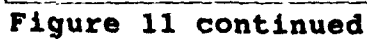


Figure 11. Bihourly model-predicted profiles of zonal velocity ($\bar{u}(z)$ solid line m/sec), temperature ($\bar{T}(z)$ dotted line degree C), downward momentum flux ($-\bar{u}w(z)$ dashed line m^2/sec^2), and dissipation ($\epsilon(z)$ chain-dot line m^2/sec^3) for day 9 of case 2.



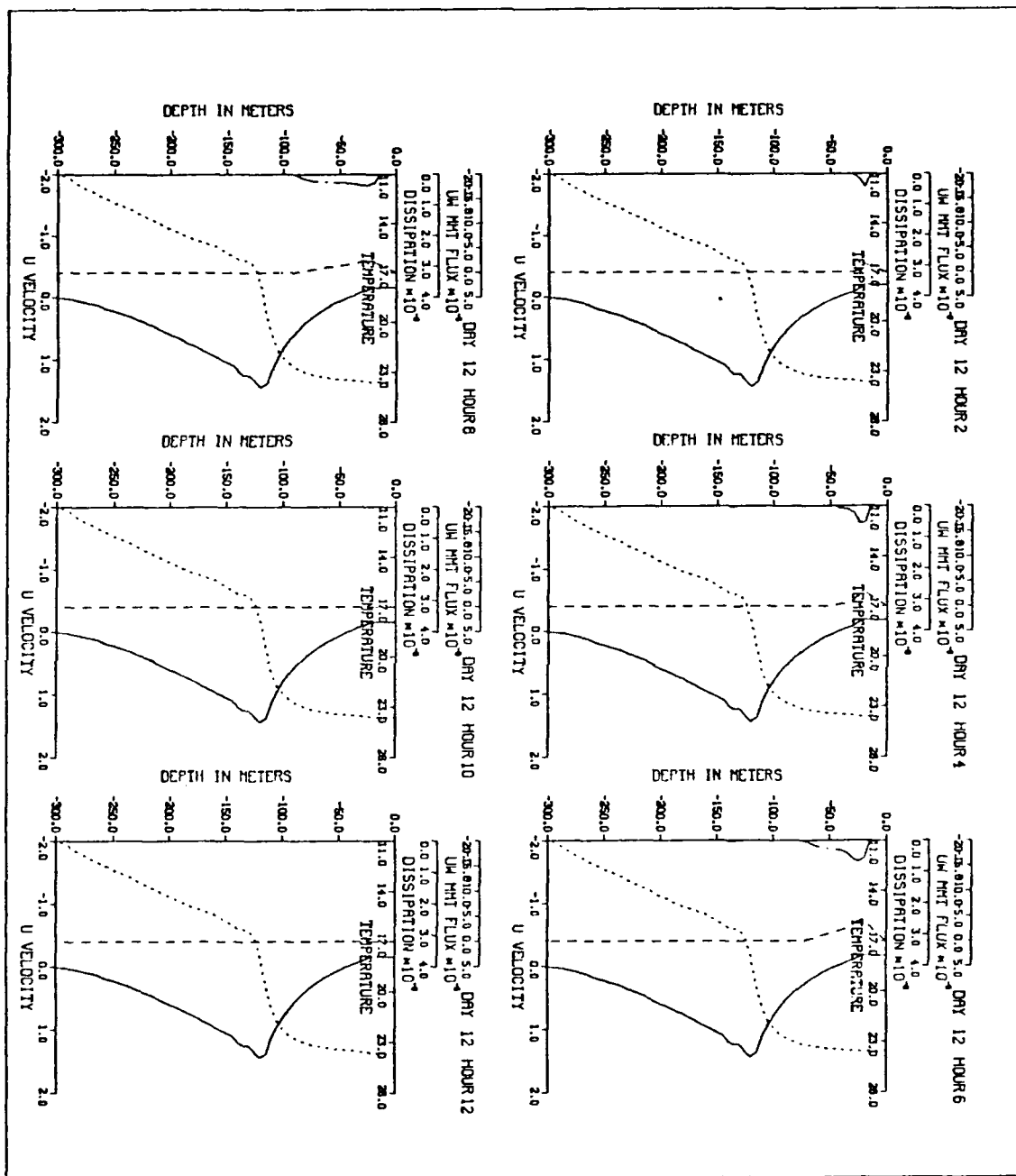


Figure 12. Bihourly model-predicted profiles of zonal velocity ($\bar{u}(z)$ solid line m/sec), temperature ($\bar{T}(z)$ dotted line degree C), downward momentum flux ($-\bar{u}'w'$ (z) dashed line m^2/sec^2), and dissipation ($e(z)$ chain-dot line m^2/sec^3) for day 12 of case 2.

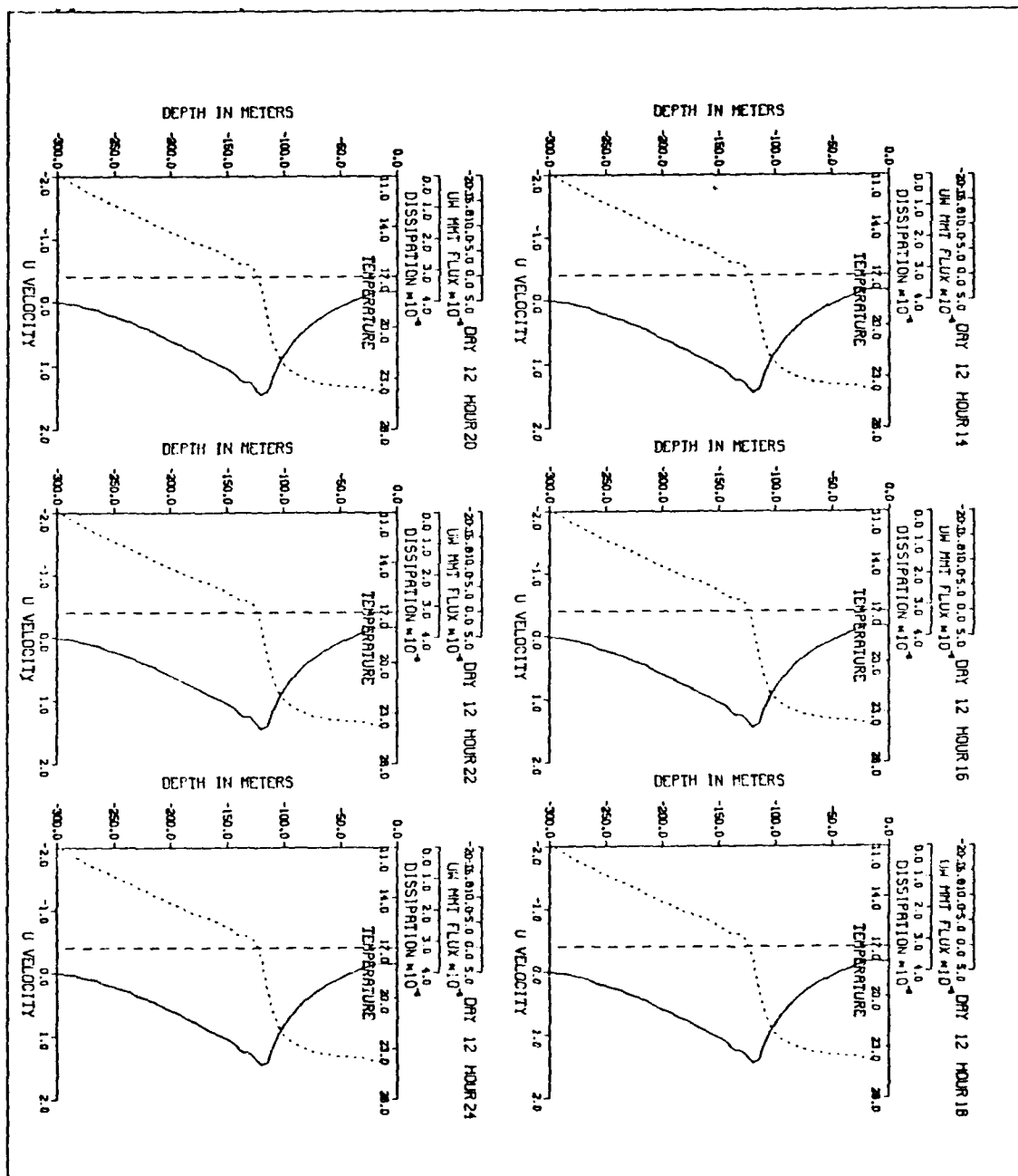


Figure 12 continued

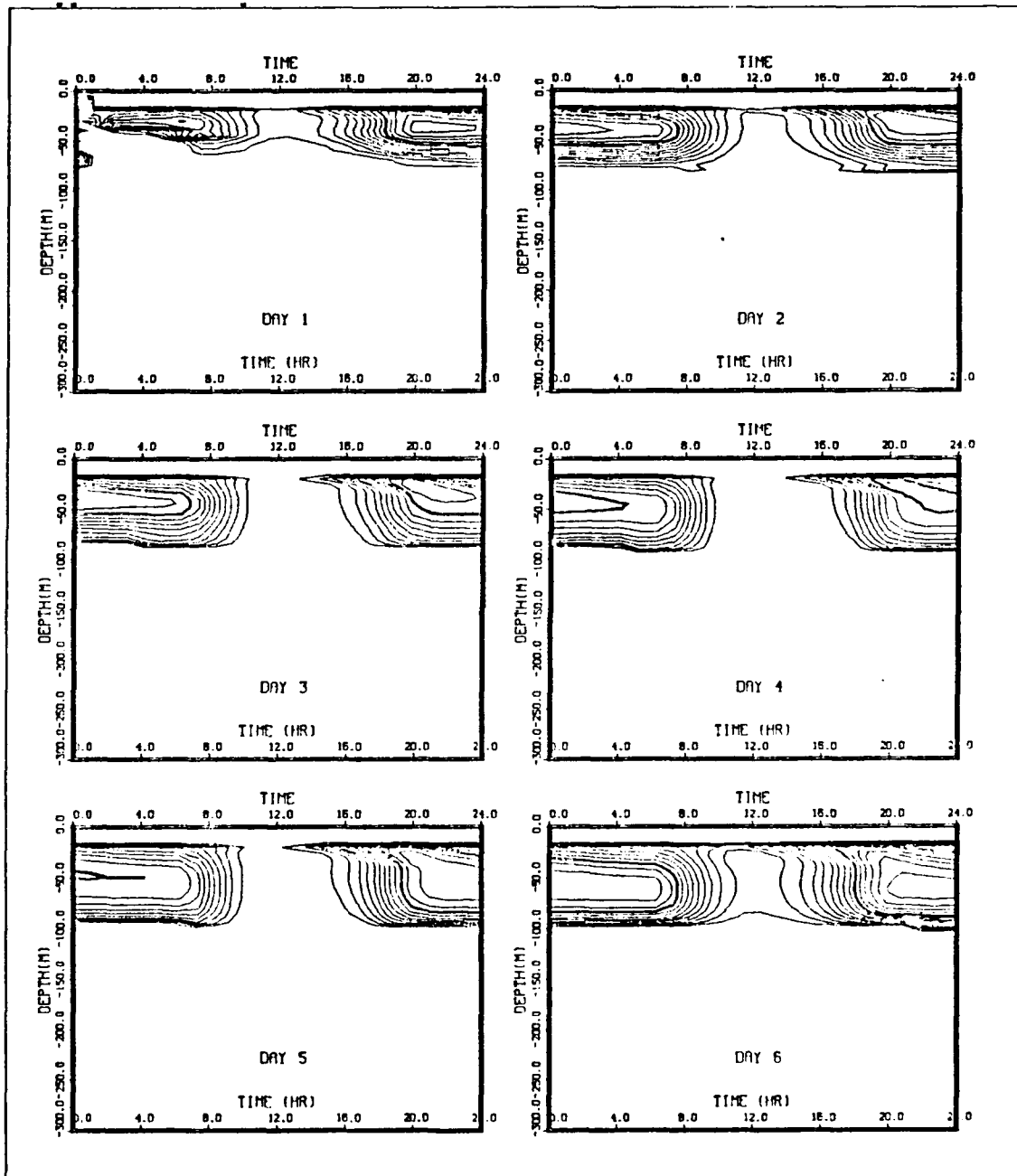


Figure 13. Predicted daily dissipation vs time and depth for case 2. The contour increment is $2 \times 10^{-7} \text{ m}^2/\text{sec}^3$. The bold line has the value of $2 \times 10^{-6} \text{ m}^2/\text{sec}^3$.

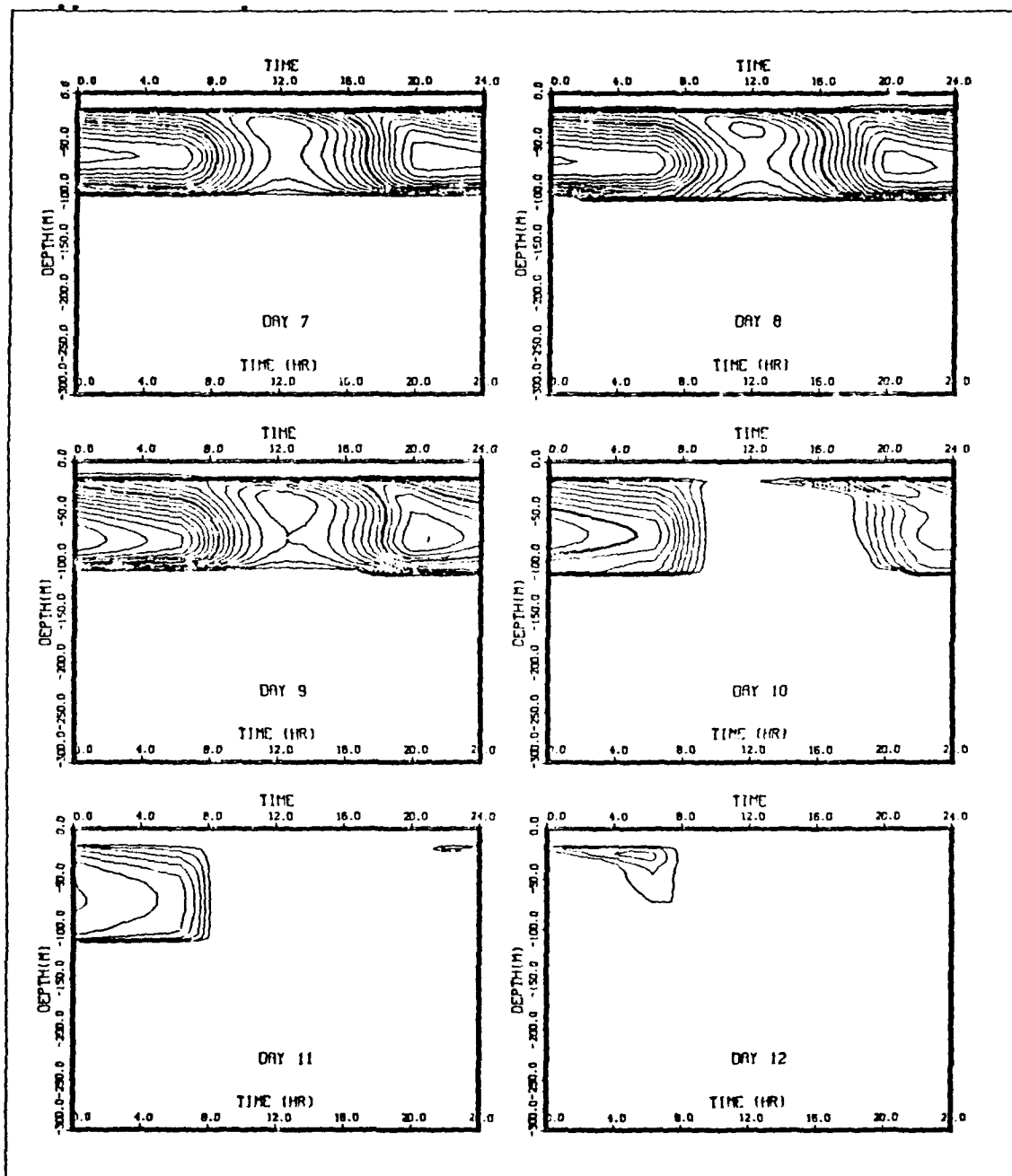


Figure 13 continued

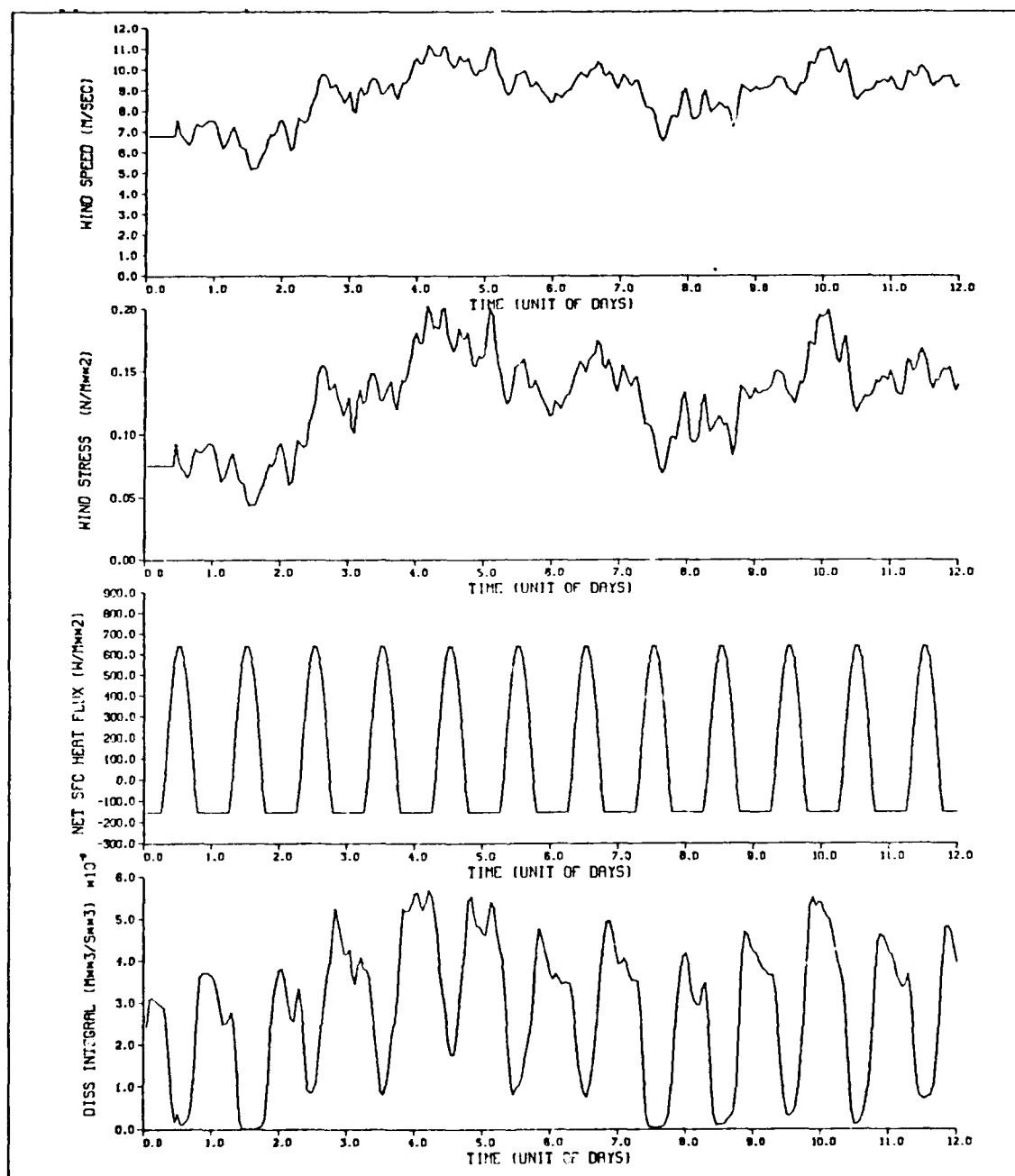


Figure 14. Surface forcing conditions of (a) recorded wind speed, (b) wind stress, (c) and net surface heat flux as in previous cases and (d) vertical integral of dissipation for case 3.

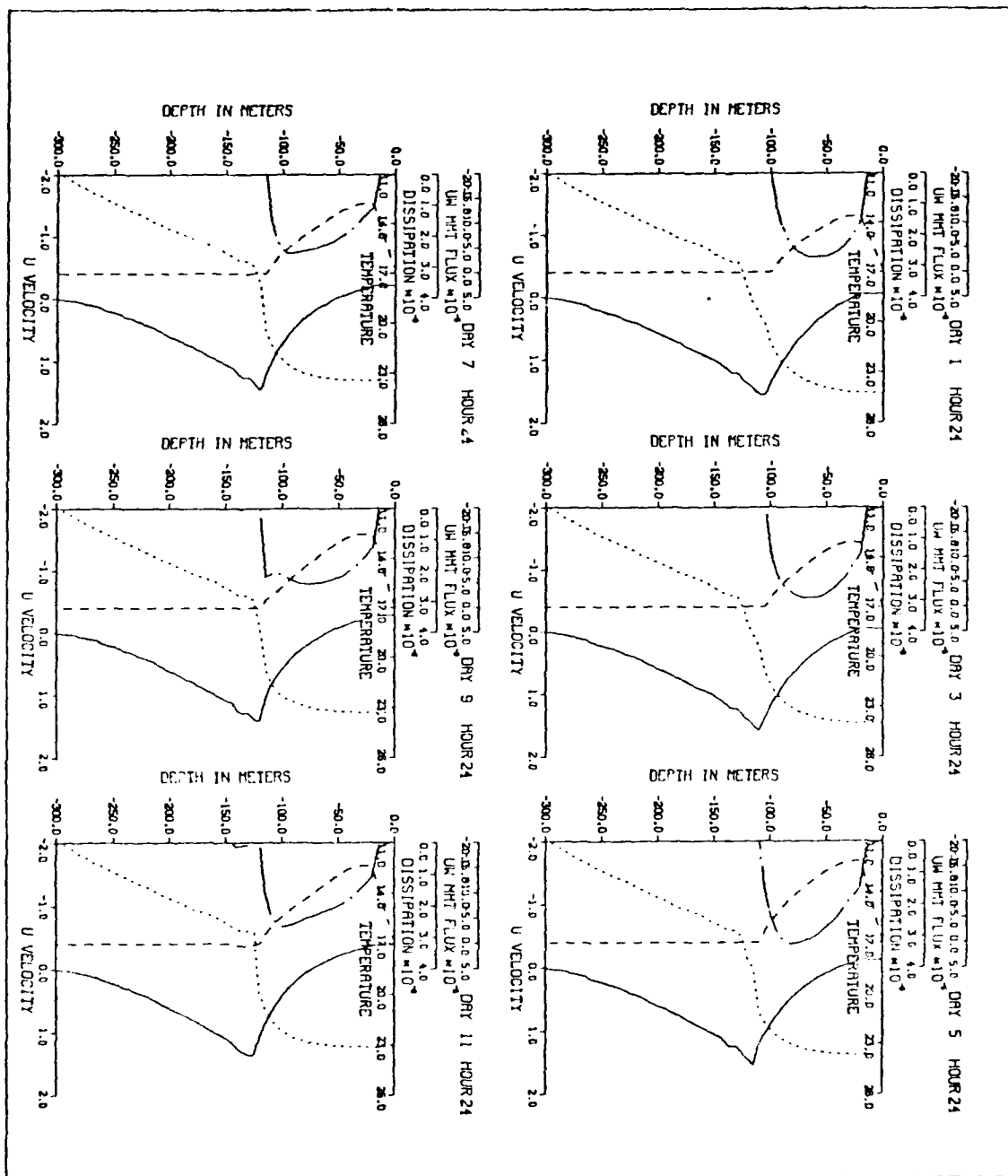


Figure 15. Bidaily model-predicted profiles of zonal velocity ($\bar{u}(z)$ solid line m/sec), temperature ($\bar{T}(z)$ dotted line degree C), downward momentum flux ($-\bar{u}'w'(z)$ dashed line m^2/sec^2), and dissipation ($\epsilon(z)$ chain-dot line m^2/sec^3) for case 3.

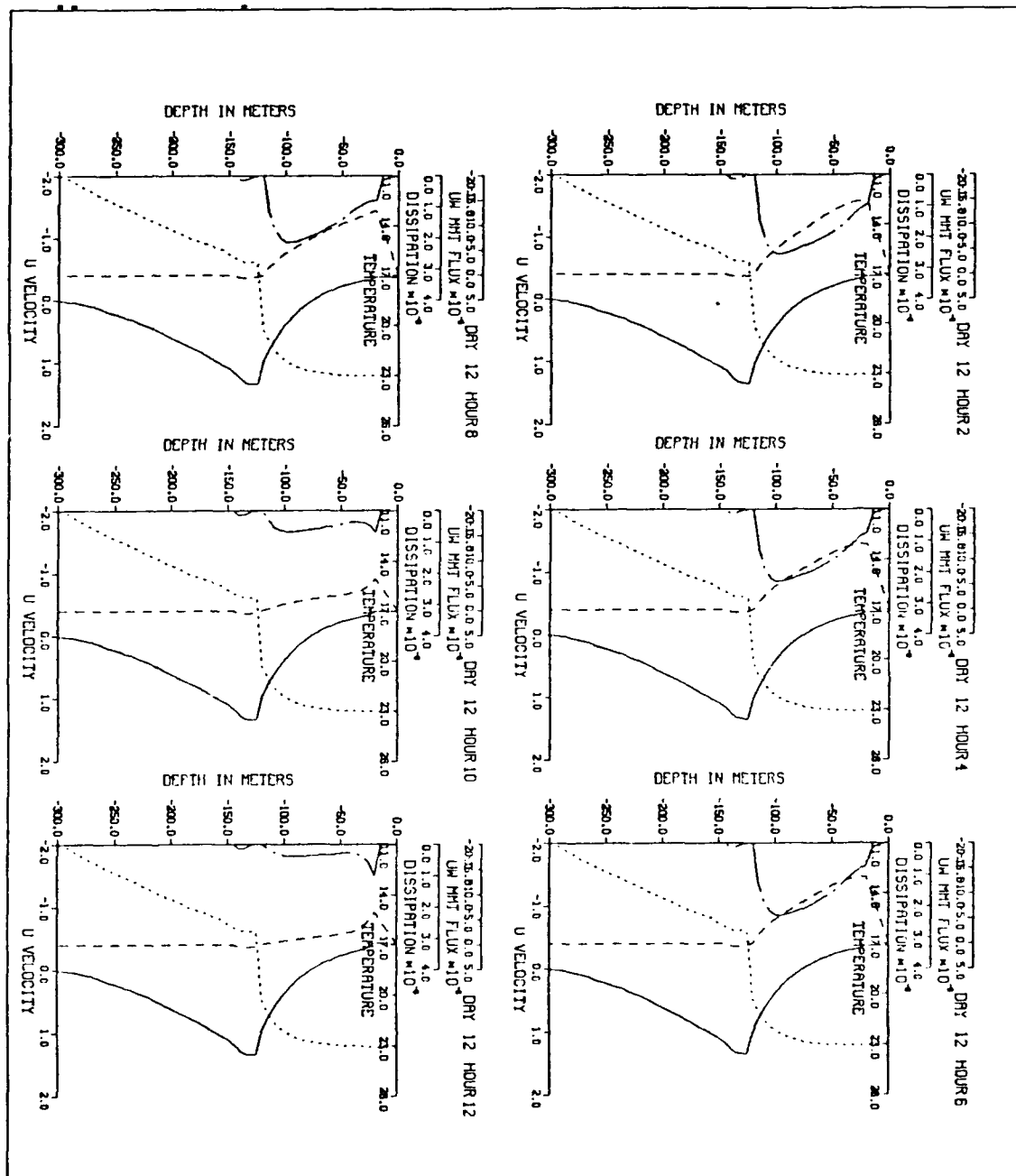


Figure 16. Bihourly model-predicted profiles of zonal velocity ($\bar{u}(z)$ solid line m/sec), temperature ($\bar{T}(z)$ dotted line degree C), downward momentum flux ($-\bar{u}'w'(z)$ dashed line m^2/sec^2), and dissipation ($e(z)$ chain-dot line m^2/sec^3) for day 12 of case 3.

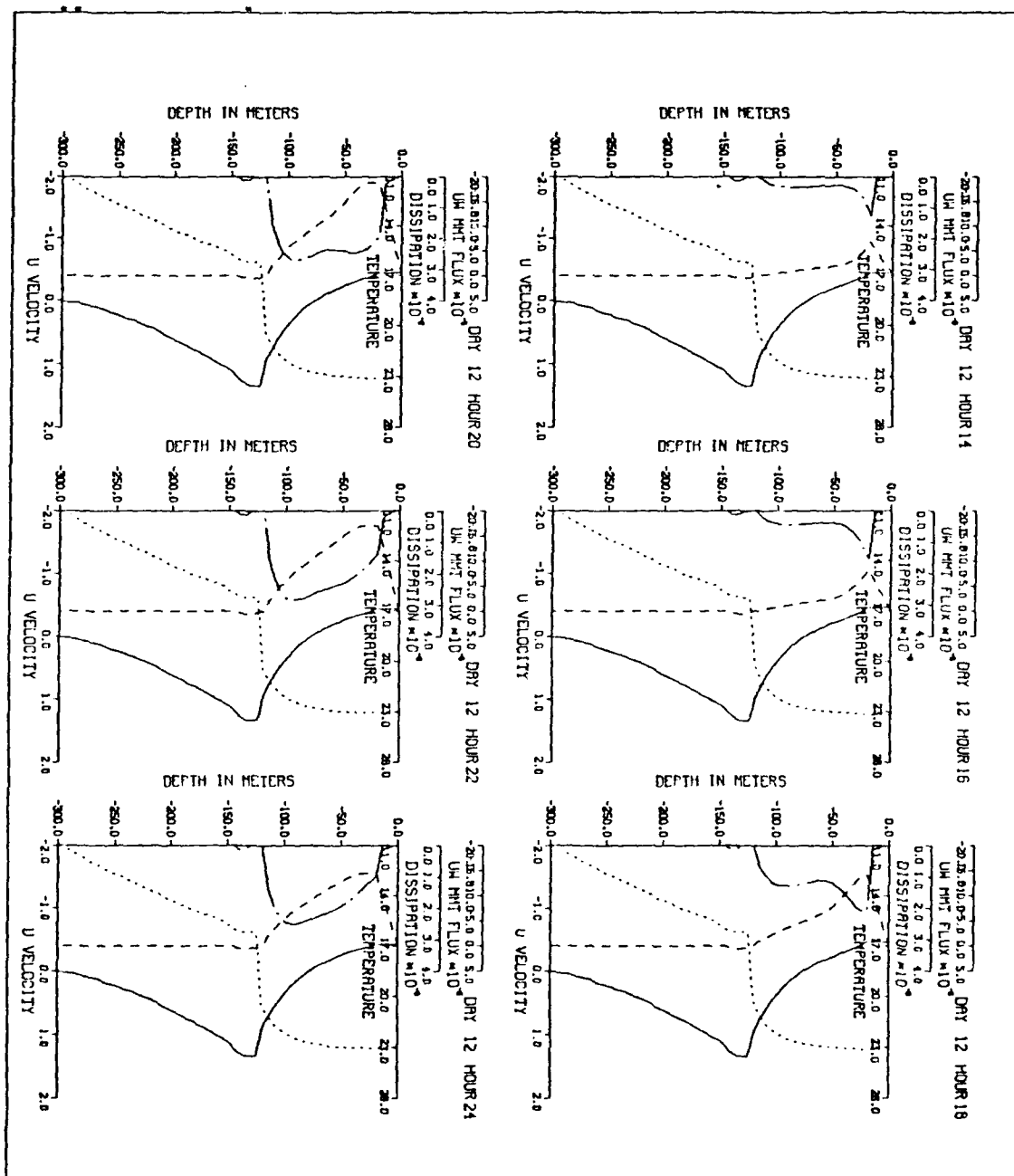


Figure 16 continued

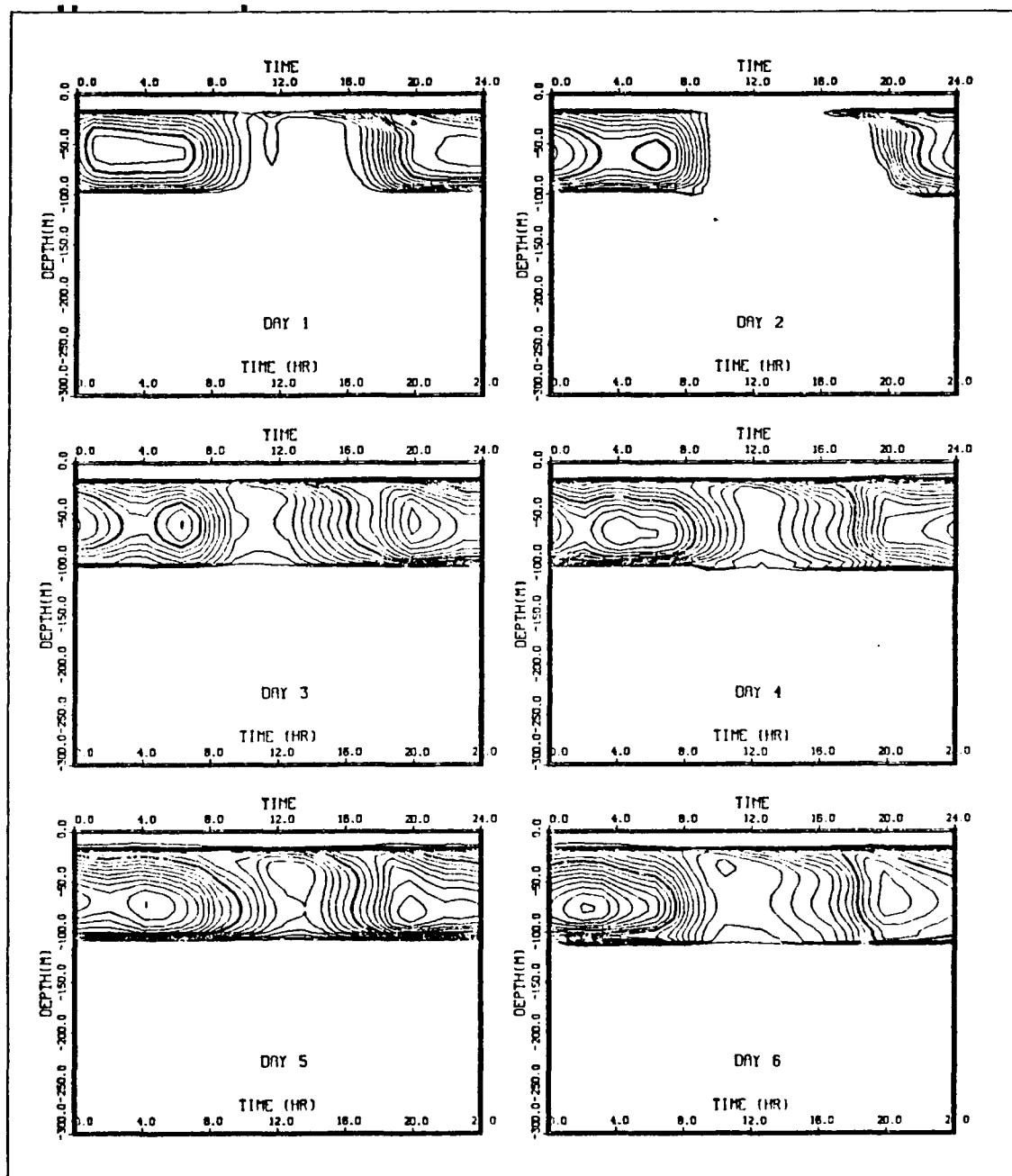


Figure 17. Predicted daily dissipation vs. t and z for case 3. The contour increment in $2 \times 10^{-7} \text{ m}^2/\text{sec}^3$

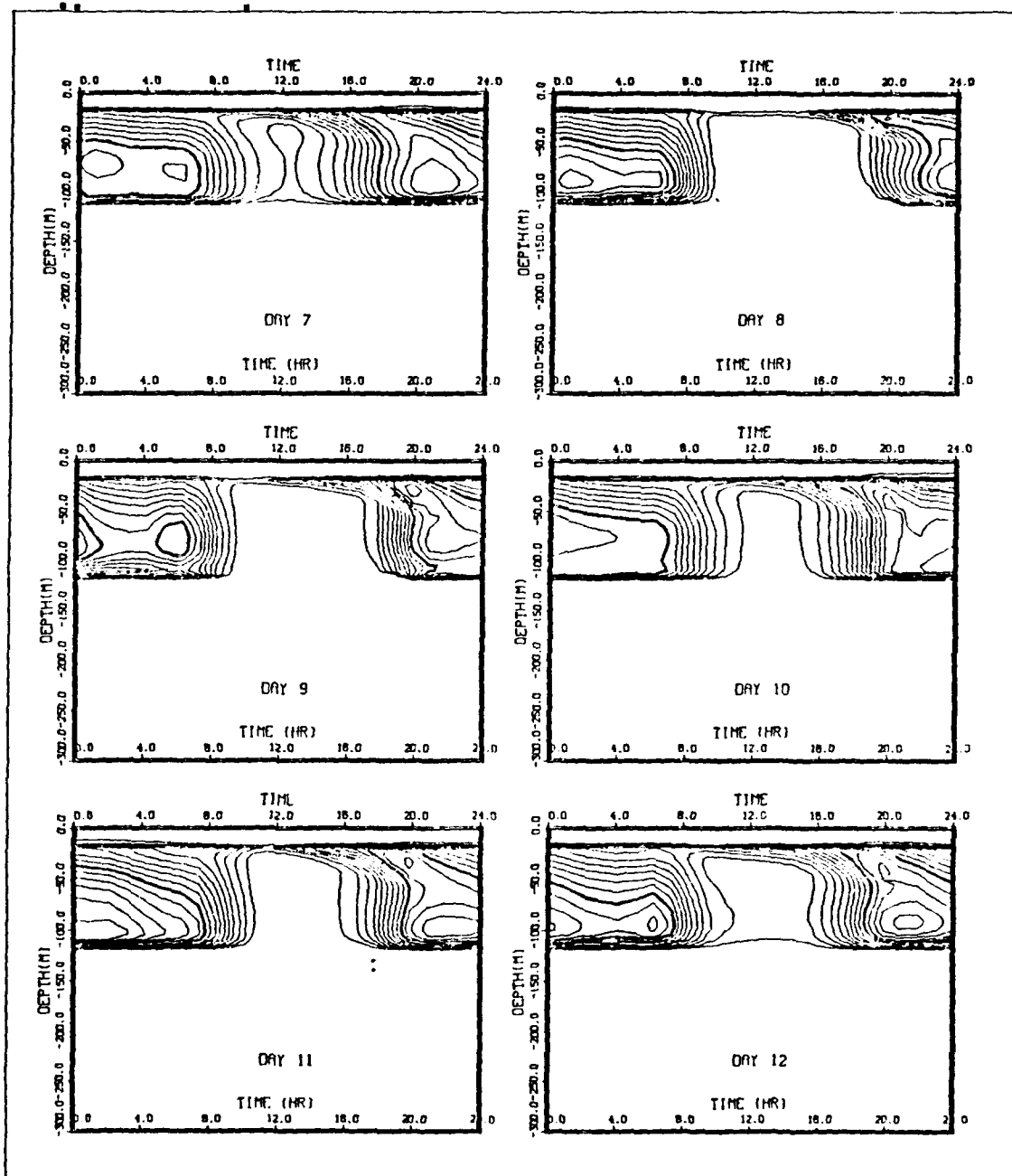


Figure 17 continued

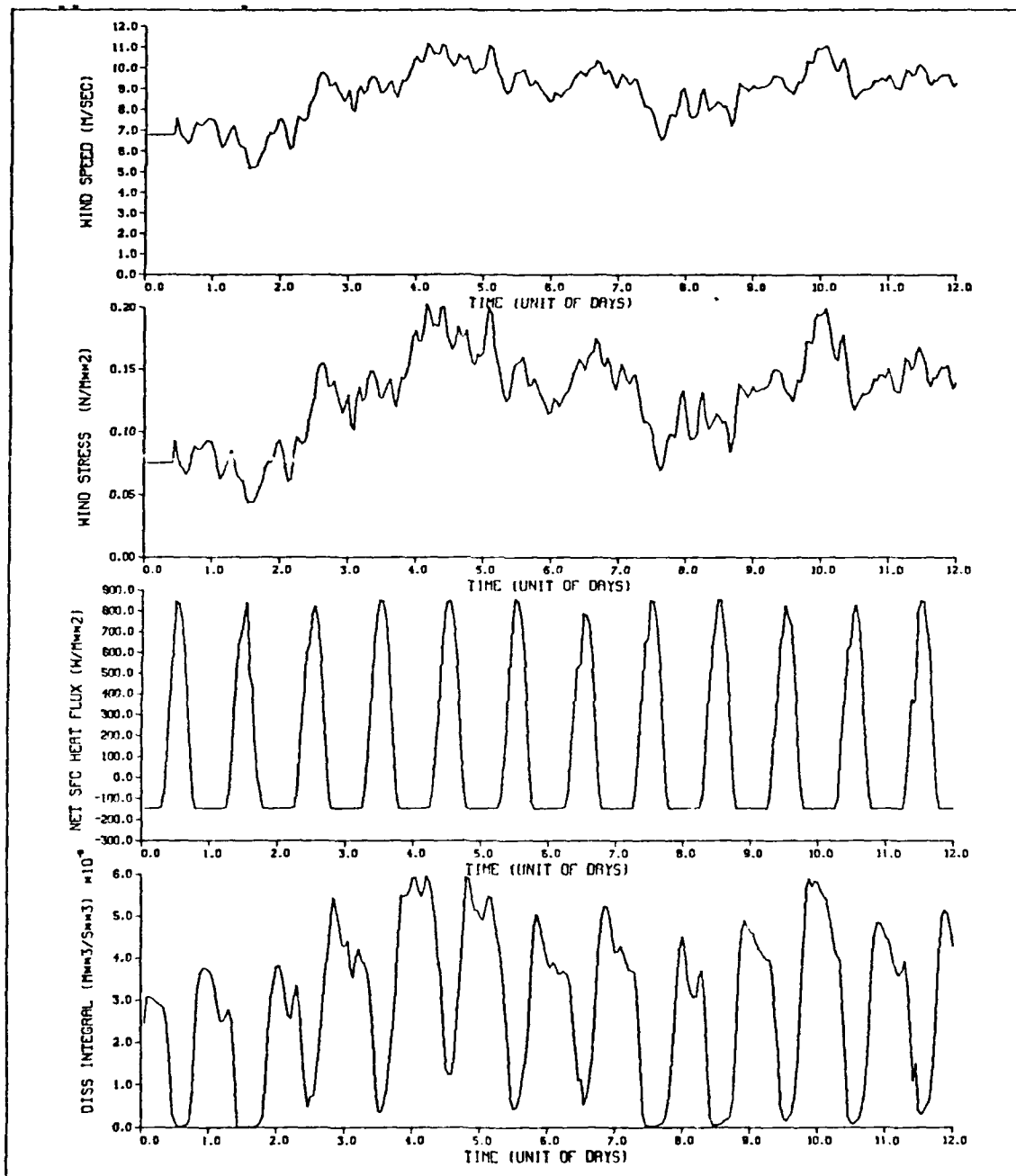


Figure 18. Surface forcing conditions and vertical integral dissipation for case 4. (a) and (b) are the same as for case 3. (c) The net surface heat flux. (d) Vertical integral of dissipation showing a lower value of dissipation in the day time.

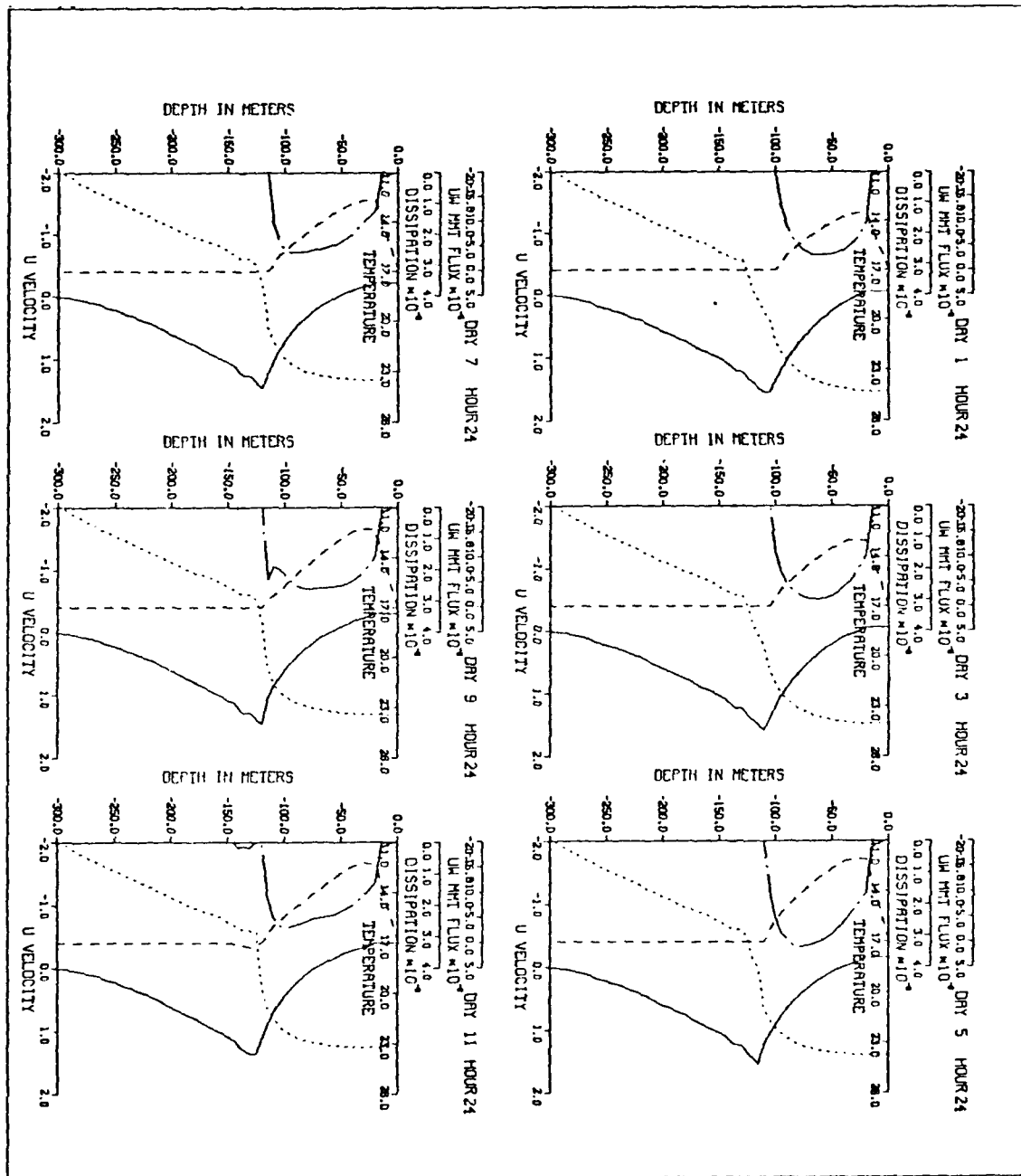


Figure 19. Bidaily model-predicted profiles of zonal velocity ($\bar{u}(z)$ solid line m/sec), temperature ($\bar{T}(z)$ dotted line degree C), downward momentum flux ($-\bar{u}w(z)$ dashed line m^2/sec^2), and dissipation ($e(z)$ chain-dot line m^2/sec^3) for case 4.

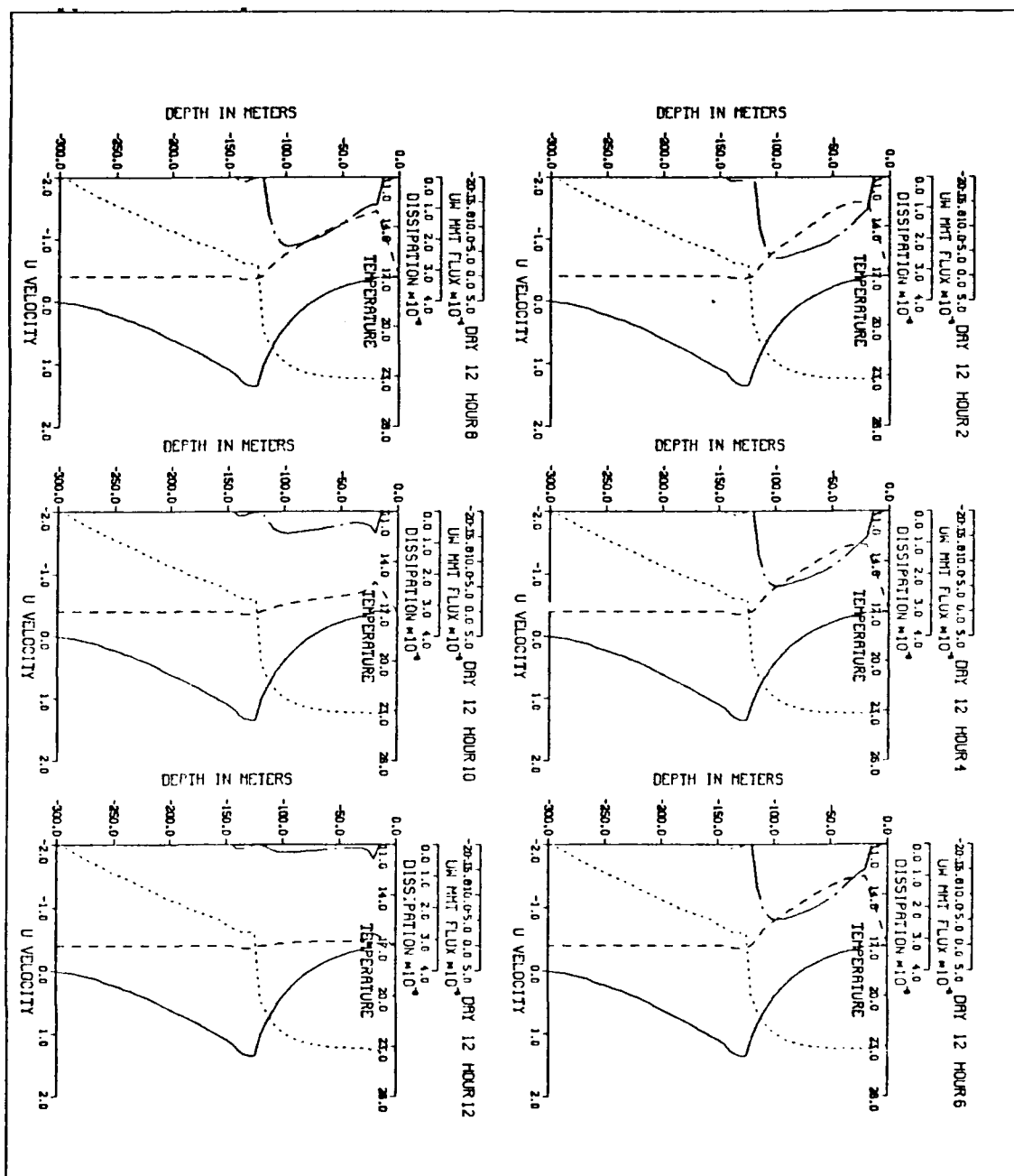


Figure 20. Bihourly model-predicted profiles of zonal velocity ($\bar{U}(z)$ solid line m/sec), temperature ($\bar{T}(z)$ dotted line degree C), downward momentum flux ($-\bar{u}'w'(z)$ dashed line m^2/sec^2), and dissipation ($\bar{e}(z)$ chain-dot line m^2/sec^3) for day 12 of case 4.

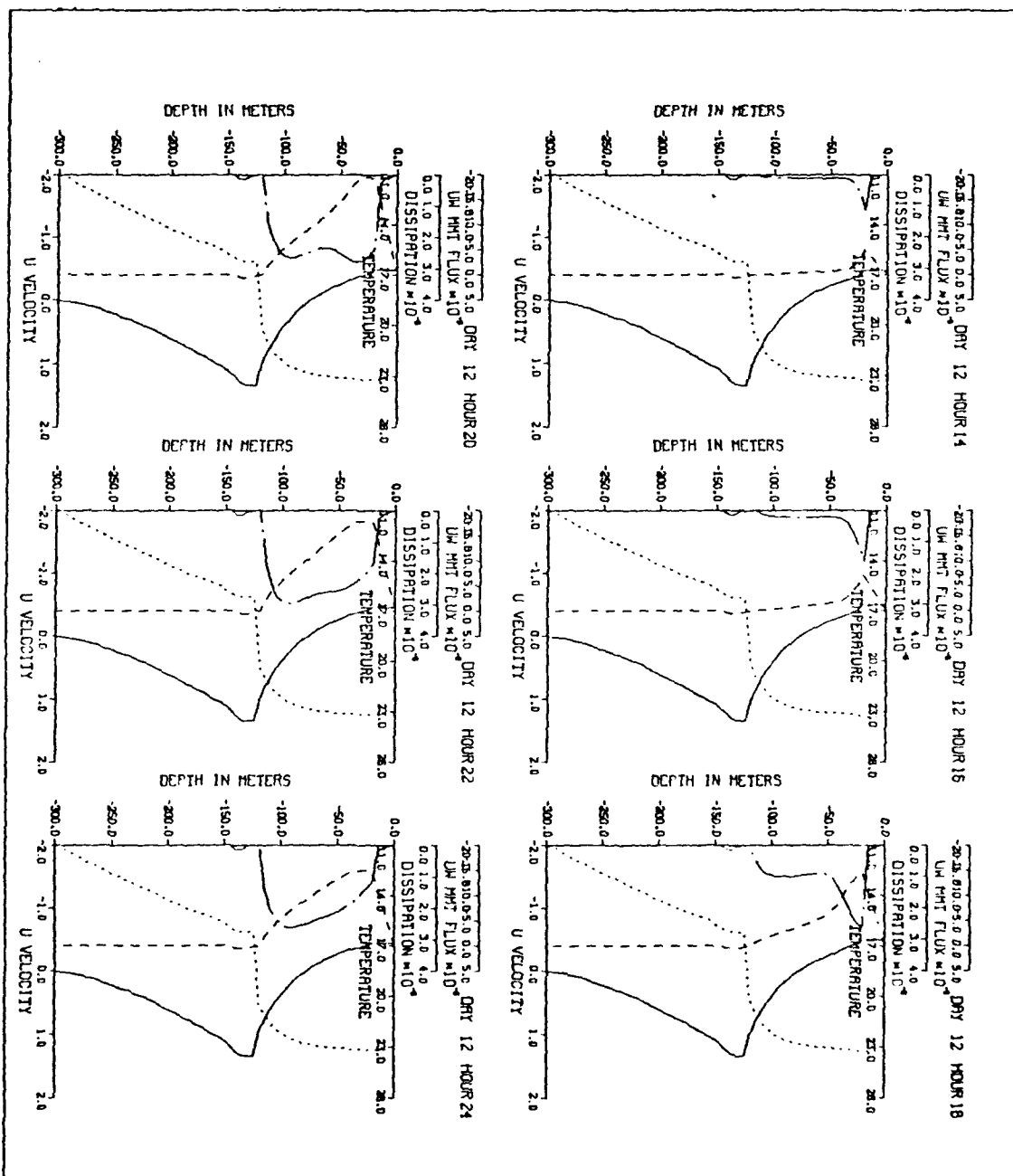


Figure 20 continued

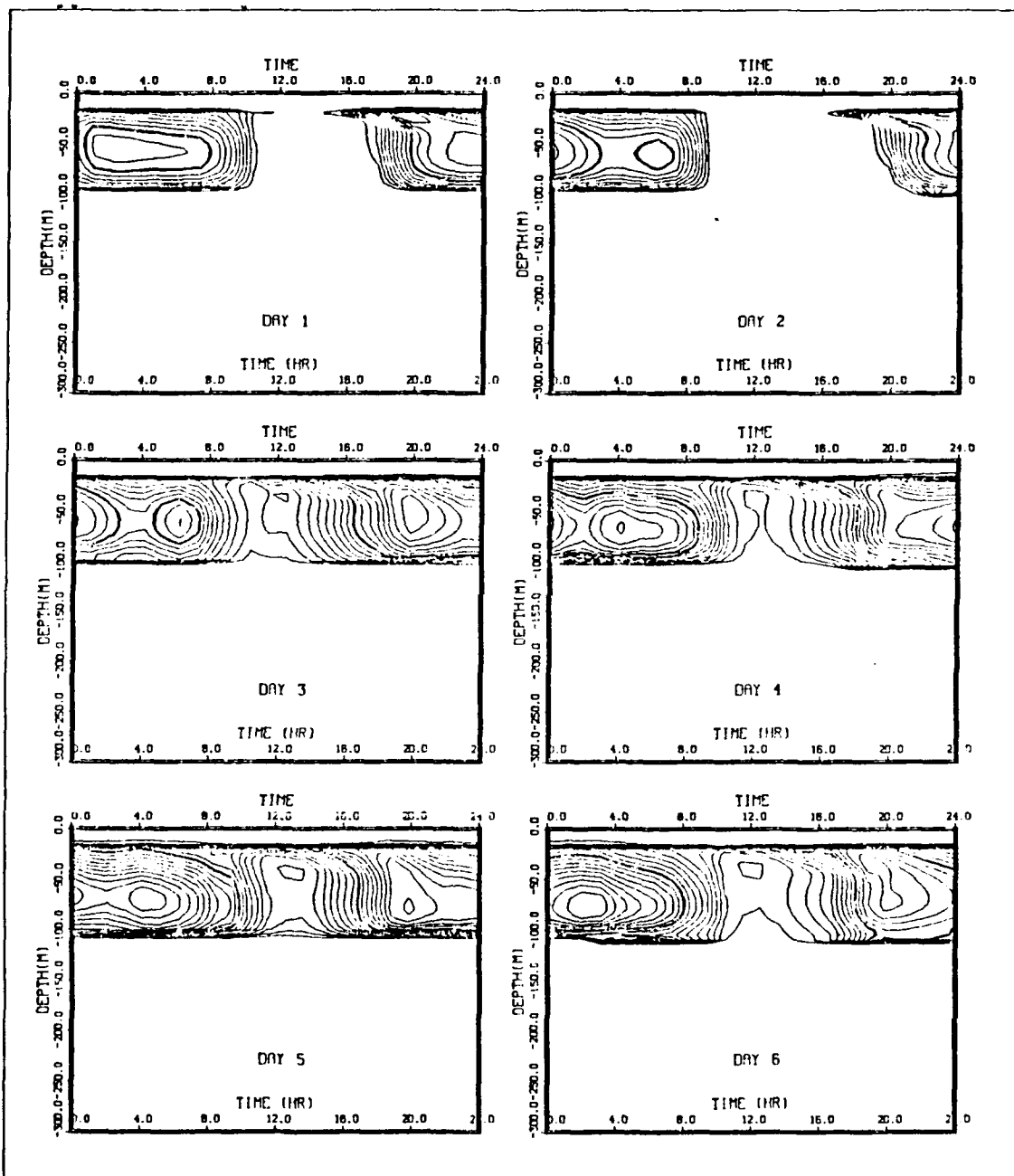


Figure 21. Predicted daily dissipation vs t and z for case 4. The contour increment is $2 \times 10^{-7} \text{ m}^2/\text{sec}^3$.

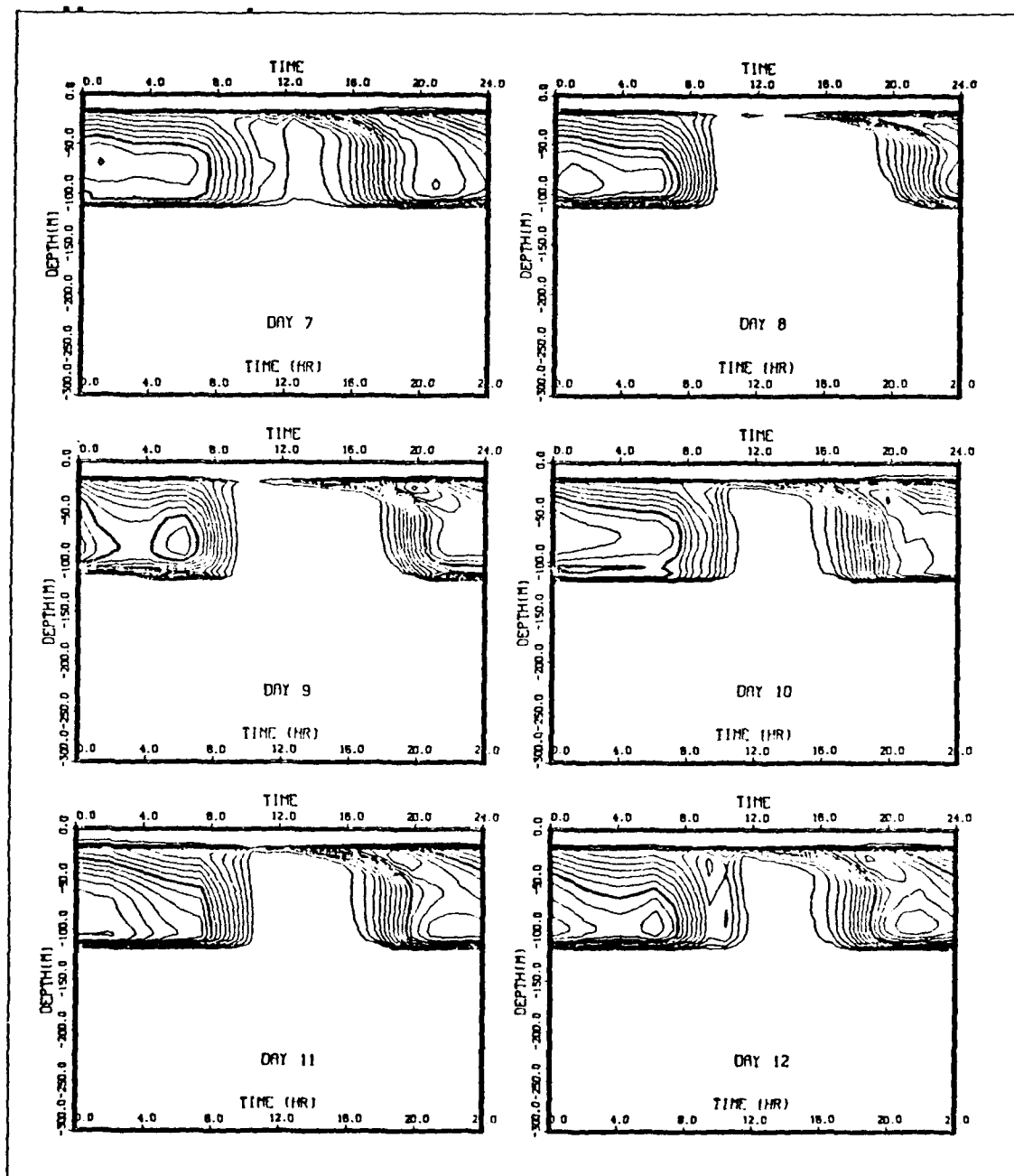


Figure 21 continued

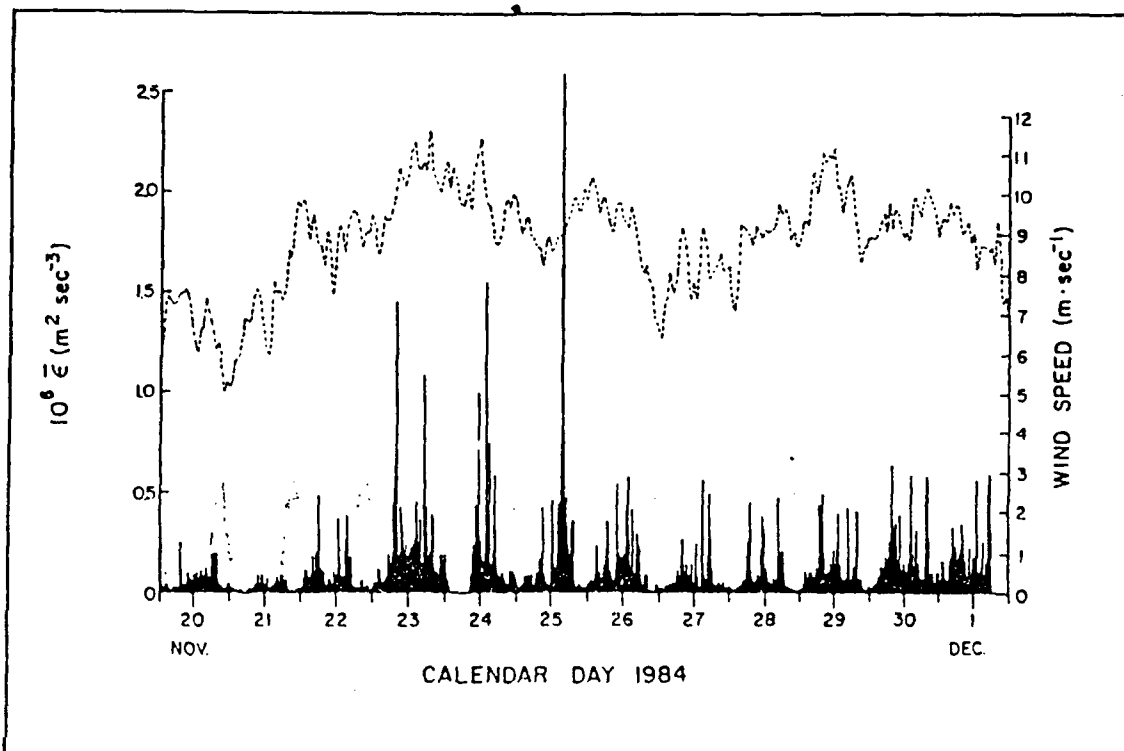


Figure 22. Depth averaged dissipation (10-110 m) observed in the Tropic I Experiment in November 1984 at equator, 140 W. The large ticks on the abscissa represent 1200 GMT (0200 LT). Hourly winds from shipboard measurement are superimposed. (From Moum et al., 1989)

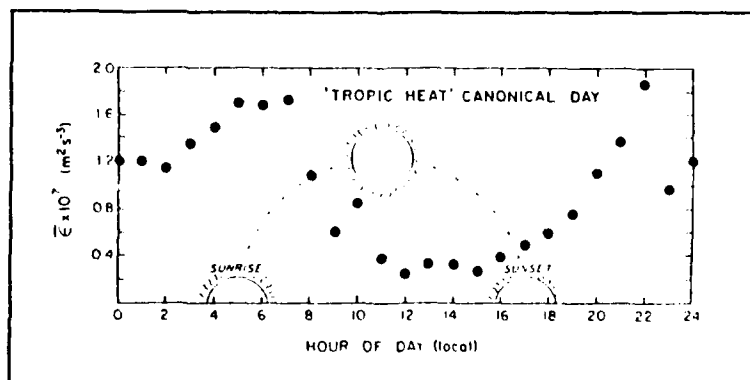


Figure 23. Ensemble averages of depth-averaged dissipation for each hour of the day from the dissipation observations in the Tropic Heat I Experiment in November 1984 (Moum et al., 1989).

IV. SUMMARY AND RECOMMENDATIONS

The purpose of this study was to investigate how the turbulent mixing and dissipation in the equatorial entrainment zone are effected by surface forcing. An equatorial entrainment zone model developed by Garwood et al. (1989) was employed to explain the effects of wind stress and surface heat flux on dissipation of turbulence. For a variety of cases, the model successfully predicts both the deep dissipation events in the equatorial entrainment zone and the diurnal dissipation cycle.

The model was forced with four different surface forcing conditions to demonstrate the relative roles of wind stress and surface heat flux on the dissipation rate. In the case of diurnally periodic solar radiation and constant wind stress (case 1), a near equilibrium state was reached by day 5. Dissipation occurs mainly above the EUC core where the vertical gradient of zonal velocity is negative and the momentum flux is downward. Therefore, a downward propagation of dissipation is reflected in the sequential dissipation profiles that show the depth of maximum dissipation to increase with time in response to changes in surface forcing. The greatest magnitude of downward momentum flux is always at 20 m, the base of the mixed layer. The vertical integral of

dissipation reaches its maximum value just before midnight and sharply decreases two hours after sunrise.

The model simulation using a linearly varying wind speed (case 2) shows the maximum magnitude of downward momentum flux at 20 m responding instantly to the wind stress. The depth of maximum dissipation is also effected by the wind. The model simulation using recorded wind (case 3) exhibits a greater depth of dissipation penetration, and a larger value of dissipation resulted from longer-lasting high wind events. The maxima of dissipation value occurring in the early morning (before sunrise) always correspond to the peaks in wind speed. However, after sunset to midnight, the maxima of dissipation values do not always correspond to higher wind events. Sometimes the dissipation maxima lag the wind fluctuation by 1-2 hours.

The model simulation using recorded wind and solar radiation (case 4) results in a larger value of buoyant damping due to stronger daytime shortwave solar heating at the sea surface. This decreases the daytime dissipation rate and increases mean kinetic energy stored in the mixed layer. After sunset, the shear production of TKE converts more mean KE into TKE, giving a higher value of dissipation rate in the entrainment zone. Dissipation is increased more in the shallow region than in the deep region. A secondary dissipation maximum under the EUC core at about 140 m depth is frequently evident. The 12-day ensemble of vertical integral of

dissipation has been averaged for each hour of the day to show dissipation differs by nearly a factor of 10 between local noon and early morning and reaches its greatest magnitude at hour 22. These modeled effects compare favorably to the observations.

This equatorial entrainment zone model based upon an assumed dynamic stability criterion explains both the unusual thickness of the entrainment zone at the equator and the potential for short-term fluctuations in surface forcing to be "felt" at a considerable depth below the mixed layer, with a phase lag that is depth dependent.

Several recommendations for further study are suggested from this work:

1. What is the appropriate value for the critical Richardson number in the entrainment zone at the equator, and is this a universal constant for all oceanic entrainment zones?
2. Does a similar dynamic instability influence the region below the undercurrent? Numerical experimentation indicates that this region may become dynamically unstable, depending upon the vertical velocity field and the baroclinicity of the flow. However, turbulence beneath the undercurrent does not appear to be as strong in this region as it is above the undercurrent core.
3. What is the role of asymmetry about the equator in the surface forcing? Meridional fluxes may be significant, and even transient meridional velocity events may have an important role in determining the equilibrium state of the mean velocity field at the equator. Therefore, more intense survey is needed and a three-dimensional model must be developed to simulate the phenomena realistically.

REFERENCES

- Adamec, D.D., R.L. Elsberry, R.W. Garwood Jr., and R.L. Hancy, 1981: An Embedded Mixed Layer Ocean Circulation Model. *Dyn. Atmos. Oceans.*, 69-96.
- Bryden, H.L., and E.C. Brady, 1985: Diagnostic Model of the Three-Dimensional Circulation in the Upper Equatorial Pacific Ocean. *J. Phys. Oceanogr.*, **15** 1255-1273.
- Crawford, W.R., and T.R. Osborn, 1981: Control of Equatorial Ocean Currents by Turbulent Dissipation. *Science*, **212**, 439-540.
- Dillon, T.M., J.N. Moum, T.K. Chereskin, and D.R. Caldwell, 1989: Zonal Momentum Balance at the Equator, *J. Phys. Oceanogr.*, **19**, 561-570.
- Elsberry, R.L., W.M. Frank, G.J. Holland, J.D. Jarrell, and Southern, R.L., 1985: *A Global View of Tropical Cyclones*, 34.
- Firing, E., 1987: Deep Zonal Currents in the Central Equatorial Pacific, *J. Mar. Res.*, **45**, 791-812.
- Firing, E., C. Fenander, and J. Miller, J., 1981: Profiling Current Meter Measurements From the NORPAX Hawaii to Tahiti Shuttle Experiment, Data Rep. 39, HIG-81-2, Hawaii Institute of Geophysics.
- Gallacher, P.C., 1987: Importance of Rotation Shear Stress for Entrainment in the Ocean Mixed Layer, Ph.D. Thesis, Naval Postgraduate School, Monterey, CA.
- Galperin, B., A. Rosati, L.H. Kantha, and G.L. Mellor, 1989: Modeling Rotating Stratified Turbulent Flows with Application to Oceanic Mixed Layers, *J. Phys. Oceanogr.*, **19** 901-916.
- Garwood, R.W. Jr., 1977: An Oceanic Mixed Layer Model Capable of Simulating Cyclic States, *J. Phys. Oceanogr.*, **7**, 455-468.
- Garwood, R.W. Jr., 1987: Unsteady Shallowing Mixed Layer, *Proceedings 'Aha Huliko'a, Hawaiian Winter Workshop*, P. Muller and D. Henderson, eds., Hawaii Institute of Geophysics Special Publication, 119-129.

Garwood, R.W. Jr., P.C. Chu, P. Muller, and N. Schneider, submitted for publication, 1989: *Modeling the Equatorial Entrainment Zone: Response to Diurnal Surface Forcing*.

Garwood, R.W. Jr., P.C. Gallacher, and P. Muller, 1985: Wind Direction and Equilibrium Mixed Layer Depth," *J. Phys. Oceanogr.*, **15**, 1332-1338.

Garwood, R.W. Jr., P. Muller, and P.C. Gallacher, 1985: Wind Direction and Equilibrium Mixed Layer Depth in the Tropical Pacific Ocean, *J. Phys. Oceanogr.*, **15** 1332-1338.

Gray, W.M.: Tropical Cyclone Genesis, Dept. of Atmospheric Science, Paper No. 232, Colorado State University: Ft. Collins, Colorado, 121.

Gregg, M.C., H. Peters, J.C. Wesson, N.S. Oakey, and T.J. Shay, 1985: Intensive Measurements of Turbulence and Shear in the Equatorial Undercurrent, *Nature*, **318**, 140-144.

Hughes, R.L., 1980: On the Equatorial Mixed Layer, *Deep-Sea Res.*, **27a**, 1067-1078.

Huschke, R.E., 1959: *Glossary and Meteorology*, American Meteorological Society, 483.

Moum, J.N., D.R. Caldwell, C.A. Paulson, 1989: Mixing in the Equatorial Surface Layer, *J. Geophys. Res.*, **94**, 2005-2021.

Moum, J.N., D.R. Caldwell, C.A. Paulson, T.K. Chereskin, and L.A. Regier, 1986: Does Ocean Turbulence Peak at the Equator? *J. Phys. Oceanogr.*, **16**, 1991-1994.

Muller, P., 1976: On the Diffusion of Momentum and Mass by Internal Gravity Waves, *J. Fluid Mech.*, **77**, 789-823.

Muller, P., and R.W. Garwood, Jr., 1988: Mixed Layer Dynamics: Progress and New Directions, *Trans. Am. Geophys. Union*, **69**, 2-12.

Muller, P., and H. Roth, 1987: On the Meridional Structure of the Equatorial Mixed Layer, *Oceanologica Acta*, **6**, 7-14.

Muller, P., R.W. Garwood, Jr., and J.P. Garner, 1984: Effect of Vertical Advection on the Dynamics of the Oceanic Surface Mixed Layer, *Annales Geophys.*, **2**, 387-398.

Munk, W.H., and E.R. Anderson, 1948: Notes on a Theory of the Thermocline, *J. Mar. Res.*, **7**, 276-295.

- Neiburger, M., J.G. Edinger, and W.D. Bonner, 1982: *Understanding Our Atmospheric Environment*, 274-277.
- Obukhov, A.M., 1971: Turbulence in an Atmosphere With a Nonuniform Temperature, *Trudy Inst. Teoret. Geofiz, AN SSSR*, I, 1946; translated and reprinted in *Bound-Layer Meteor.*, 2.
- Pacanowski, R.C., and S.G.H. Philander, 1981: Parameterization of Vertical Mixing in Numerical Models of Tropical Oceans, *J. Phys. Oceanogr.*, 11, 1443-1451.
- Paka, V.T., and K.N. Fedorov, 1982: Influence of the Thermal Structure of the Upper Ocean Layer on the Development of Turbulence, *Izvest. Atmos. Ocean Phys.*, 18, 134-138.
- Peters, H., M.C. Gregg, and J.M. Toole, 1988: On the Parameterization of Equatorial Turbulence, *J. Geophys. Res.*, 93, 1199-1218.
- Peters, H., M.C. Gregg, and J.M. Toole, 1989: Meridional Variability of Turbulence Through the Equatorial Undercurrent, *J. Geophys. Res.*, 94, 18003-18010.
- Rossby, C.G., and R.B. Montgomery, 1935: The Layer of Frictional Influence in Wind and Ocean Currents, *Pap. Phys. Oceanogr. Meteor.*, 3, 101.
- Schopf, P.S., and M.A. Cane, 1983: On Equatorial Dynamics, Mixed Layer Physics and Sea Surface Temperature, *J. Phys. Oceanogr.*, 13, 917-935.
- Tchernia, P., 1980: *Descriptive Regional Oceanography*, 226, plate 12.
- Weare, B.C., P.T. Strub, and M.D. Samuel, 1981: Annual Mean Surface Heat Fluxes in the Tropical Pacific Ocean, *J. Phys. Oceanogr.*, 11, 705-717.
- Wyrtki, K., 1981: An Estimate of Equatorial Upwelling in the Pacific, *J. Phys. Oceanogr.*, 11, 1204-1214.
- Wyrtki, K., 1978: Monitoring the Strength of Equatorial Currents From XBT Sections and Sea Level, *J. Geophys. Res.*, 83, 1935-1940.
- Wyrtki, K., 1984: Mean Water and Current Structure During the Hawaii-to-Tahiti Shuttle Experiment, *J. Phys. Oceanogr.*, 14, 242-253.
- Wyrtki, K., and G. Meyers, 1976: The Trade Wind Field Over the Pacific Ocean, *J. Appl. Meteor.*, 15, 694-704.

INITIAL DISTRIBUTION LIST

	No.Copies
1. Defense Technical Information Center Cameron Station Alexandria, VA 22304-6145	2
2. Library, Code 0142 Naval Postgraduate School Monterey, CA 93943-5002	2
3. LCDR Chi-Shao Chen #44 Lane 29 PAI-JEN St. Hsing-Tien Taipei, Taiwan R.O.C.	6
4. Library Chinese Naval Academy Kaoshiung, Taiwan R.O.C.	1
5. Department of Oceanography Naval Postgraduate School Monterey, CA 93943-5000 Attn: Chairman (Code 68/Co) Dr. R.W. Garwood (Code 68/Gd) Dr. P.C. Chu (Code 68/Cu) CDR F.Y. Kuo (SMC 2303) LCDR C.L.Tan (SMC 1135) LCDR B.K. Wu (SMC 1427)	1 2 1 1 1 1
6. Department of Meteorology Naval Postgraduate School Monterey, CA 93943-5000 Attn: Chairman (Code 63/Rd) Dr. R.L. Haney (Code 63/Hy) LCDR T.C. Yin (SMC 2408) LCDR C. Liu (SMC 2138)	1 1 1 1
7. Commanding Officer Navy Headquarters Taipei, Taiwan, ROC	1
8. Commanding Officer Naval Hydrographic & Oceanographic Office Tso-Ying, Kaoshinng, Taiwan, ROC	1

- | | | |
|-----|--|---|
| 9. | Department of Oceanography
National Taiwan University
Taipei, Taiwan, ROC | 1 |
| 10. | Department of Oceanography
National Chung San University
Kaoshinng, Taiwan, ROC | 1 |
| 11. | Director .aval Oceanography Division
Naval Observatory
34th and Massachusetts Avenue NW
Washington, D.C. | 1 |
| 12. | Commander
Naval Oceanography Command
NSTL Station
Bay St. Louis, MS 39522 | 1 |
| 13. | Commanding Officer
Naval Oceanographic Office
NSTL Station
Bay St. Louis, MS 39522 | 1 |
| 14. | Commanding Officer
Fleet Numerical Oceanography Center
Monterey, CA 93943 | 1 |
| 15. | Commanding Officer
Naval Ocean Research and Development Activity
NSTL Station
Bay St. Louis, MS 39522 | 1 |
| 16. | Office of Naval Research (Code 1120PO)
800 N. Quincy Street
Arlington, VA 22217 | 1 |
| 17. | Commanding Officer
Naval Environmental Prediction Research Facility
Monterey, CA 93943 | 1 |
| 18. | Chairman, Oceanography Department
U.S. Naval Academy
Annapolis, MD 21402 | 1 |
| 19. | Scientific Liaison Office
Office of Naval Research
Scripps Institution of Oceanography
La Jolla, CA 92037 | 1 |

- | | | |
|-----|---|---|
| 20. | Commander
Oceanographic Systems Pacific
Box 1390
Pearl Harbor, HI 96960 | 1 |
| 21. | Commanding Officer
Naval Eastern Oceanography Center
Naval Air Station
Norfolk, VA 23511 | 1 |
| 22. | Commanding Officer
Naval Western Oceanography Center
Box 113
Pearl Harbor, HI 96860 | 1 |
| 23. | Commanding Officer
Naval Oceanography Command Center, Rota
Box 31
FPO New York, NY 09540 | 1 |